International Journal of Mechanical Sciences 140 (2018) 557–580

Contents lists available at ScienceDirect

International Journal of Mechanical Sciences

journal homepage: www.elsevier.com/locate/ijmecsci

Stable discontinuous space–time analysis of dynamic interface crack growth in orthotropic bi-materials using oscillatory crack tip enrichment functions

Arman Afshar, Saeed Hatefi Ardakani, Soheil Mohammadi*

High Performance Computing Laboratory, School of Civil Engineering, University of Tehran, Tehran, Iran

ARTICLE INFO

Keywords:
Dynamic interface crack growth
Stable discontinuous space–time analysis
Oscillatory crack velocity dependent fields
Orthotropic bi-materials

ABSTRACT

The problem of dynamic interface crack propagation in layered composites is addressed in this paper. Recently developed dynamic orthotropic bi-material enrichment functions are utilized to allow for accurate capturing of the oscillatory stress and displacement fields near the interface crack tip and proper evaluating of the crack tip velocity. The time discontinuous finite element and balance of recovery methods are employed during the crack propagation process in order to increase the stability and accuracy of the solution in dynamic crack propagation problems. Also, a suitable crack propagation criterion and an iterative algorithm are used to determine the interface crack tip velocity in each time step. Fracture mechanics parameters, such as dynamic stress intensity factor, phase angle and energy release rate are accurately predicted using the interaction integral method and the crack velocity dependent auxiliary fields. Numerical simulations of dynamic crack propagation in a homogeneous isotropic material, dynamic interface crack propagation in an isotropic bi-material, and dynamic interface crack propagation in an orthotropic bi-material are performed and the predictions are compared with the reference experimental and analytical results and the numerical data available in the literature.

1. Introduction

Today, thin layer orthotropic composite materials are extensively being used in various industries due to their high strength-to-weight ratio. However, intrinsic defects present in these materials may limit their use in sensitive applications, making fracture analysis an important part of reliability estimation of structures made from these composites. Interface cracks are among the most critical defects as they can easily contribute to catastrophic failure. Impact loading, in particular, can cause progressive interface crack propagation and structural failure during manufacture and service of composite materials. Hence, this paper is dedicated to present a novel and accurate simulation of dynamic interface crack propagation in composite materials.

Several analytical, experimental and numerical techniques are available for modeling of dynamic fracture problems [1–7]. Analytical solutions have limitations in treating problems with realistic complex geometries and loading conditions [3,7]. Experimental methods for analyzing dynamic crack propagation under impact loading require special expensive equipment for applying the load and recording the results. On the other hand, numerical methods in general and the finite element method (FEM) in particular are very efficient and capable of accurate modeling of complex geometries and loadings. In problems of crack growth, however, the efficiency and accuracy of conventional FEM decrease as adaptive remeshing and fine meshes are generally required.

Increasing the number of elements in the crack tip region and remeshing techniques substantially increase the computational cost in a dynamic simulation; requiring development of new approaches.

The extended finite element method (XFEM), developed to overcome the shortcomings of FEM [8], employs the enrichment functions to model the discontinuities within a cracked element and singularity near a crack tip. Alternatively, the extended isogeometric analysis (XIGA) adopts the conventional enrichment functions within the NURBS-based isogeometric formulation to capture the discontinuities within a cracked element and the singularity near a crack tip [9–12].

Another approach, the phase field model is an efficient method for prediction of strong discontinuity (crack) nucleation and direction of crack extension [13,14]. The rate-dependent phase field approach, by which the crack tip velocity is accurately evaluated [14], can be used to solve dynamic crack propagation problems.

In this study, the extended finite element method is utilized to simulate the dynamic interface crack growth in orthotropic bi-materials. In the case of stationary crack, several studies have been conducted on the static and dynamic fracture analysis of composites using XFEM [15–23]. In the work by Asadpoure and Mohammadi [15], new enrichment functions were presented for XFEM analysis of crack in orthotropic media. Esna Ashari and Mohammadi introduced oscillatory enrichment functions for static analysis of interface cracks in orthotropic bi-materials [16], and Afshar et al. [24] used these functions to analyze

* Corresponding author.
E-mail address: smoham@ut.ac.ir (S. Mohammadi).

https://doi.org/10.1016/j.ijmecsci.2018.03.031
Received 12 November 2017; Received in revised form 7 March 2018; Accepted 24 March 2018
Available online 27 March 2018

stationary interface cracks in orthotropic bi-materials under dynamic loadings. Also, Afshar et al. recently investigated the fracture response of interface crack tip in shape memory alloy/elastic bi-materials [25]. In addition, several XFEM simulations have been performed to study the dynamic fracture of piezoelectric and magnetoelectroelastic solids [26–28]. Bui and Zhang used XFEM analysis to investigate the dynamic stress intensity factors for stationary cracks in piezoelectric and magnetoelectroelastic materials [26,27]. For the case of functionally graded piezoelectric solids, Liu et al. developed an XFEM model to transiently analyze stationary cracks in these materials [28].

In the case of static crack propagation, quite a number of works, all of which present an XFEM approach to reproduce the displacement and stress fields near the crack tip, are available in the literature [29–31]. XFEM has also performed quite well in dynamic crack propagation problems. Belytschko et al. presented an XFEM method for dynamic crack propagation based on the loss of hyperbolicity criterion [32]. Chessa and Belytschko presented an XFEM formulation in time and space for dynamic problems with arbitrary discontinuities [33,34]. Also, Belytschko and Chen introduced a singular element for dynamic crack growth problems [35]. Moreover, the problem of crack arrest was addressed by Grégoire et al. [36], and Haboussa et al. [37] investigated the effects of crack-hole interaction. In another interesting study, Combescure et al. [38] studied the concept of energy conservation in dynamic XFEM. Finally, Menouillard et al. [39] proposed a novel mass lumping strategy for explicit integration in dynamic XFEM. While the mentioned studies were all conducted on homogeneous isotropic materials, Motamedi and Mohammadi [40,41] applied the dynamic XFEM for analysis of dynamic crack propagation in orthotropic materials. In addition, Kumar et al. [42] proposed new XFEM enrichment functions to study the dynamic fracture behavior of cracked homogeneous solids and bi-material composites. They concluded that using Heaviside and cubic ramp enrichment functions would result in better solution than using other enrichment functions in the cases of stationary and moving dynamic cracks.

A difficulty in the analysis of dynamic crack propagation is the choice of time integration method in order to solve the dynamic equations in a stable manner. The widely used Newmark method is suitable for dynamics problems with stationary cracks [24]; however, it results in spurious numerical oscillations in dynamic crack propagation problems. These oscillations substantially increase the possibility of instability in the solution. An effective method for stable solutions is the time discontinuous finite element method, proposed by Li et al. [43] and Rethore et al. [44]. In this method, enriched shape functions are added to the time finite element method in order to consider the time discontinuity in the dynamic equation, resulting in more stable solutions. Therefore, this integration method is chosen here to deal with the problem of interface crack growth.

Another crucial issue in simulating dynamic crack propagation problems is the estimation of crack tip velocity. While many studies assume crack velocity a priori, a suitable criterion and an iterative algorithm are used here to determine the interface crack tip velocity during the simulation. To our best knowledge, this is the first time that such an accurate simulation is adopted for modeling interface crack propagation without requiring the crack tip velocity in advance.

The present study is indeed an extension of the work conducted by Afshar et al. [24] in order to investigate dynamic crack propagation in homogeneous isotropic materials, dynamic interface crack propagation in isotropic bi-materials, and dynamic interface crack propagation in orthotropic bi-as. New velocity dependent oscillatory crack-tip enrichment functions are proposed in the framework of XFEM methodology to reproduce the exact distribution of oscillatory crack velocity dependent fields around the interface crack tip, resulting in improvement in stability and accuracy of the solution. Moreover, a suitable crack propagation criterion and an iterative algorithm are presented to determine the interface crack tip velocity.

Organization of this paper is as follows: in Section 2, the mechanical behavior of composite materials is provided. Dynamic interface fracture mechanics formulation, based on linear elastic fracture mechanic (LEFM), is discussed in Section 3. Section 4 describes the criteria for estimating the interface crack velocity and Section 5 briefly discusses XFEM formulation in space and crack velocity dependent enrichment functions. Moreover, the time discontinuous finite element method for time integration of dynamic equation, numerical implementations of the iterative algorithm for estimating the crack velocity, and the balance of recovery algorithm are presented to complete the formulation. Finally, Section 6 presents the numerical examples of dynamic crack propagation in different materials: homogeneous, isotropic and orthotropic bi-materials, along with the investigation of effects of the oscillatory crack tip fields and the stabilizing algorithms. The paper closes with the concluding remarks.

2. Governing equation

The strong form of the governing equation for a two-dimensional dynamic problem of an orthotropic layered medium (Ω) with an initial interface crack (Γ_c) can be written as:

$$\nabla.\boldsymbol{\sigma} + \rho\mathbf{b} = \rho\ddot{\mathbf{u}} \text{ in } \Omega \tag{1}$$

where ρ is the density, $\boldsymbol{\sigma}$ is the stress tensor and $\mathbf{b}$ is the body force vector. As presented in Fig. 1, the boundary and initial conditions are considered as,

$$\mathbf{u}(\mathbf{x},t) = \bar{\mathbf{u}}(\mathbf{x},t) \text{ on } \Gamma_u \tag{2}$$

$$\boldsymbol{\sigma}.\mathbf{n} = \bar{\mathbf{t}} \text{ on } \Gamma_t \tag{3}$$

$$\boldsymbol{\sigma}.\mathbf{n} = 0 \text{ on } \Gamma_c \tag{4}$$

$$\mathbf{u}(\mathbf{x},0) = \mathbf{u}_0 \tag{5}$$

$$\dot{\mathbf{u}}(\mathbf{x},0) = \dot{\mathbf{u}}_0 \tag{6}$$

The linear stress–strain relationship for an orthotropic material can be written as [45]:

$$\begin{Bmatrix}\varepsilon_{11}\\ \varepsilon_{22}\\ 2\varepsilon_{12}\end{Bmatrix} = \begin{bmatrix}a_{11} & a_{12} & a_{16}\\ a_{21} & a_{22} & a_{26}\\ a_{61} & a_{62} & a_{66}\end{bmatrix}\begin{Bmatrix}\sigma_{11}\\ \sigma_{26}\\ \sigma_{12}\end{Bmatrix} = \begin{bmatrix}D_{1111} & D_{1122} & 2D_{1112}\\ D_{2211} & D_{2222} & 2D_{2212}\\ 2D_{1211} & 2D_{1222} & 4D_{1212}\end{bmatrix} \begin{Bmatrix}\sigma_{11}\\ \sigma_{22}\\ \sigma_{12}\end{Bmatrix} \rightarrow \text{for plane stress} \tag{7}$$

$$\left.\begin{Bmatrix}\varepsilon_{11}\\ \varepsilon_{22}\\ 2\varepsilon_{12}\end{Bmatrix} = \begin{bmatrix}b_{11} & b_{12} & b_{16}\\ b_{21} & b_{22} & b_{26}\\ b_{61} & b_{62} & b_{66}\end{bmatrix}\begin{Bmatrix}\sigma_{11}\\ \sigma_{22}\\ \sigma_{12}\end{Bmatrix} \rightarrow \text{for plane strain}\right\} \quad b_{ij} = a_{ij} - \frac{a_{i3}-a_{3i}}{a_{33}} i,j = 1,2,6 \tag{8}$$

where ε_{ij}, σ_{ij} and D_{ijkl} are the components of strain, stress, and compliance tensors, respectively.

3. Interface fracture mechanics

Dynamic stress intensity factors K_1 and K_2 for an interface crack are defined as a complex number $\mathbf{K}$ [46]:

$$\mathbf{K} = K_1 + \mathrm{i}K_2 = \lim_{r\to 0}\sqrt{2\pi r}r^{-\mathrm{i}\varepsilon}\left(\sigma_y + \mathrm{i}\frac{1}{\eta}\tau_{xy}\right)_{\theta=0} \tag{9}$$

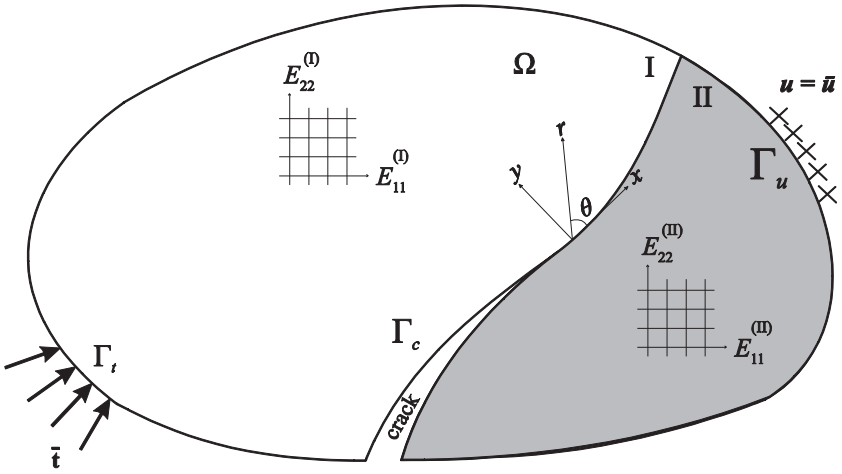

Fig. 1. An orthotropic bi-material domain Ω including an interface crack: geometry and boundary conditions.

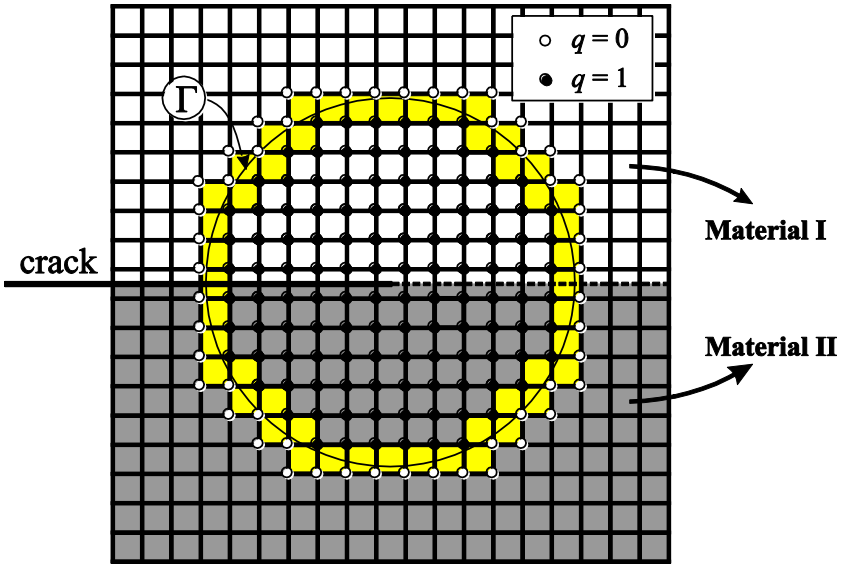

Fig. 2. Nodal values of q in the finite element mesh.

where ε and η are the oscillatory index and the resolution factor, respectively,

$$\varepsilon = \frac{1}{2\pi} \ln\left(\frac{1-\beta}{1+\beta}\right) \tag{10}$$

$$\eta = \sqrt{\frac{h_{22}}{h_{11}}} \tag{11}$$

$$\beta = \frac{h_{11}}{\sqrt{h_{12}h_{21}}} \tag{12}$$

β is Dundur's parameter, which is defined in terms of the Hermitian matrix components h_{ij}, comprehensively discussed by Nakamura et al. [47].

The energy release rate G is related to the dynamic complex stress intensity factor by

$$G = \frac{h_{21}|\mathbf{K}|^2}{4\cosh^2(\pi\varepsilon)} \tag{13}$$

The phase angle ψ, which is an index of the mode-mixity, can be written as:

$$\psi(L) = \text{Arctan}\left(\frac{\tau_{xy}}{\eta\sigma_y}\right)_{r=L} = \text{Arctan}\left(\frac{\text{Im}\left[\mathbf{K}L^{i\varepsilon}\right]}{\text{Re}\left[\mathbf{K}L^{i\varepsilon}\right]}\right) \tag{14}$$

where L is the characteristic length.

The dynamic stress intensity factors K_1 and K_2 can be determined using the interaction integral method [16,47–49]. In this study, the interaction integral formulation proposed by Nakamura et al. [47] is adopted:

$$M = \int_{\Gamma} \left[\left(\boldsymbol{\sigma} : \boldsymbol{\varepsilon}^{\text{aux}} + \rho\frac{\partial \mathbf{u}}{\partial t} \cdot \frac{\partial \mathbf{u}^{\text{aux}}}{\partial t}\right) n_1 - \left(\boldsymbol{\sigma} \cdot \frac{\partial \mathbf{u}^{\text{aux}}}{\partial x_1} + \boldsymbol{\sigma}^{\text{aux}} \cdot \frac{\partial \mathbf{u}}{\partial x_1}\right) \cdot \mathbf{n}\right] d\Gamma \tag{15}$$

where the superscript aux corresponds to the auxiliary case and $\mathbf{n}$ is the unit normal to the integration path Γ. The auxiliary stress and displacement fields are selected to satisfy the equilibrium equation and the traction-free conditions on the crack surfaces. These fields for the case of an interface crack between two orthotropic materials are reported in Appendix A. The final equivalent domain form of Eq. (15) can be written as [50],

$$M = \int_{A} \left[\left(\boldsymbol{\sigma} \cdot \frac{\partial \mathbf{u}^{\text{aux}}}{\partial x_1} + \boldsymbol{\sigma}^{\text{aux}} \cdot \frac{\partial \mathbf{u}}{\partial x_1}\right)\frac{\partial q}{\partial \mathbf{x}} - \left(\boldsymbol{\sigma} : \boldsymbol{\varepsilon}^{\text{aux}} + \rho\frac{\partial \mathbf{u}}{\partial t} \cdot \frac{\partial \mathbf{u}^{\text{aux}}}{\partial t}\right)\frac{\partial q}{\partial x_1}\right.$$
$$\left. + \left(\rho\frac{\partial^2 \mathbf{u}}{\partial t^2} \cdot \frac{\partial \mathbf{u}^{\text{aux}}}{\partial x_1} + \frac{\partial \boldsymbol{\sigma}^{\text{aux}}}{\partial \mathbf{x}} \cdot \frac{\partial \mathbf{u}}{\partial x_1} - \frac{\partial^2 \mathbf{u}}{\partial t \partial x_1} \cdot \frac{\partial \mathbf{u}^{\text{aux}}}{\partial t} - \frac{\partial \mathbf{u}}{\partial t} \cdot \frac{\partial^2 \mathbf{u}^{\text{aux}}}{\partial t \partial x_1}\right) q\right] dA \tag{16}$$

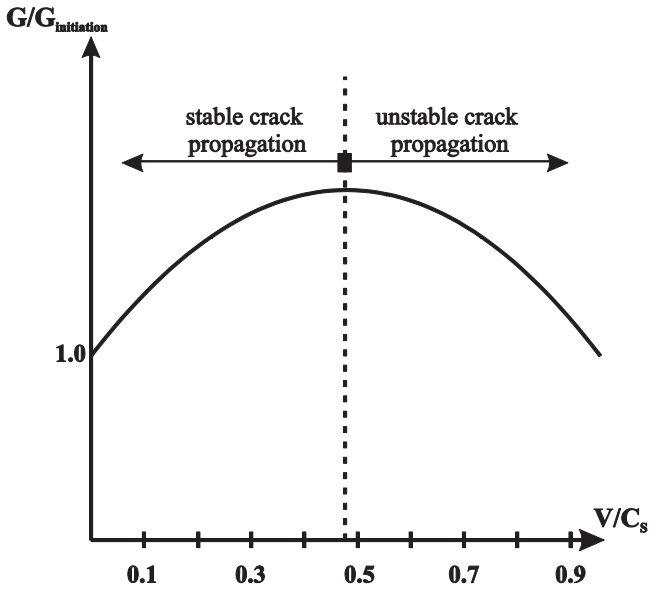

Fig. 3. Typical dependence of the energy release rate on the crack velocity (stable and unstable crack propagation modes). Note that the behavior changes at about half of the shear wave speed.

where A is the surface around the crack tip surrounded by contour Γ, as depicted in Fig. 2. q is an arbitrary smooth function, which is zero for the nodes located on or outside of Γ, and is unity for other nodes (see Fig. 2). Values of q at gauss points of elements are determined using the element shape functions,

$$q(\mathbf{x}) = \sum_{i=1}^{nn} N_i(\mathbf{x}) q_i \tag{17}$$

where nn is the number of nodes of the element, and N_i is the standard finite element shape function.

After calculating the interaction integral (16), the dynamic stress intensity factors are determined from,

$$\begin{cases} M = \frac{h_{21}}{2\cosh^2(\pi\varepsilon)} K_1(K_1^{\text{aux}} = 1; K_2^{\text{aux}} = 0) \\ M = \frac{h_{21}}{2\cosh^2(\pi\varepsilon)} K_2(K_1^{\text{aux}} = 0; K_2^{\text{aux}} = 1) \end{cases} \tag{18}$$

4. Dynamic interface crack propagation criteria

Crack tip velocity is an important parameter which determines the crack tip position at any time of a crack propagation analysis. In addition, interface crack tip fields depend on crack tip velocity. Therefore, an accurate prediction of crack tip velocity is crucial for a dynamic fracture analysis.

In order for a crack to start propagation, the energy release rate G must be greater than a critical value, associated with the dynamic crack initiation toughness. This initiation toughness is related to the physical properties of the interface between the two materials. According to [36], the dynamic interface crack growth criterion can be stated as,

$$\begin{cases} G < G_c^* \text{ Stationary crack} \\ G = G_c^* \text{ Initiation} \\ G > G_c^* \rightarrow G(V) = G_c(V) \text{ Propagation} \end{cases} \tag{19}$$

where V is the crack velocity.

As long as the energy release rate G is less than its corresponding critical dynamic crack initiation value (G_c^*), the crack remains stationary. As more energy is provided by the external loading, the energy release rate increases to the initiation toughness, starting the crack propagation. During the crack propagation state, the energy release rate at any moment remains equal to the critical dynamic energy release rate $G_c(V)$.

It should be noted that both the energy release rate and the toughness are functions of the crack velocity, and the crack tip velocity at each time step is calculated by equating the energy release rate and the corresponding critical value.

The function $G_c(V)$ must be selected properly to accurately predict the crack velocity in a numerical simulation. For a crack in a homogeneous body, the following form is widely used:

$$G_c(V) = \frac{G_c^*}{1 - \left(\frac{V}{C_R}\right)} \tag{20}$$

where C_R is the Rayleigh wave velocity.

According to the research conducted by Singh et al. [51] and Kavaturu and Shukla [52], the dynamic energy release rate can be an ascending or descending function of the crack velocity. As shown in Fig. 3, if the energy release rate is an ascending function of the crack velocity ($dG/dV > 0$), the crack propagation is stable, whereas if the energy release rate is a descending function of the crack velocity ($dG/dV < 0$), the crack propagation becomes unstable. The function $G_c(V)$ must contain both the stable and unstable modes to correctly predict the crack velocity in numerical simulations. Different forms of the function $G_c(V)$ for an interface crack are available in the literature. Nakamura et al. presented the following function $G_c(V)$ for the interface crack [47]:

$$G_c(V) = \frac{G_c^* \left(1 - \sqrt{V/C_s}\right)^{\gamma}}{1 + (\lambda - 1)\sin^2(\Psi)} \tag{21}$$

where C_s is the shear wave velocity, and Ψ is the phase angle. Constants γ and λ are obtained from fitting with available experimental data, as defined in [47].

It should be noted that Nakamura et al. [47] selected this form without any experimental basis, solely due to its descending dependence on the crack velocity. This form cannot correctly predict the crack velocity, as will be shown in the numerical examples.

Another function, based on impact experiments, is proposed by Lambros and Rosakis [53]:

$$G_c(V) = C_1^2 \frac{(1 + 4\varepsilon^2)}{4h_{21}} \left(\frac{\pi}{2a_c}\right) \tag{22}$$

where a_c is the characteristic length, and C_1 is a constant. This relationship is based on the assumption of constant ratio of shearing to opening displacement at distance a_c behind the crack tip (see Fig. 4):

$$\left.\frac{\Delta_1}{\Delta_2}\right|_{r=a_c} = \text{Constant} \tag{23}$$

The main disadvantage of function (22) is that it is only a descending function of the crack velocity. Therefore, it cannot accurately predict the crack velocity at the beginning of the crack propagation, i.e., when the crack velocity is roughly less than half the shear wave velocity.

Kavaturu and Shukla [52] changed the fundamental assumption of the form in Eq. (23) (Lambros and Rosakis [53]) and proposed an exponential increase in the opening displacement at distance a_c behind the crack tip with the crack velocity:

$$\Delta_2|_{r=a_c} = C_2 (V/C_s)^n \tag{24}$$

where C_2 and n are constants. As a result, Eq. (22) can then be rewritten as:

$$G_c(V) = C^2 \left(\frac{V}{C_s}\right)^{2n} \frac{(1 + 4\varepsilon^2)}{4h_{21}} \left(\frac{\pi}{2a_c}\right) \tag{25}$$

This experimentally supported function, which includes both stable and unstable crack growths, is adopted in this study for the first time. Numerical examples in Section 6 prove the accuracy of this function compared with other functions used in previous numerical simulations available in the literature.

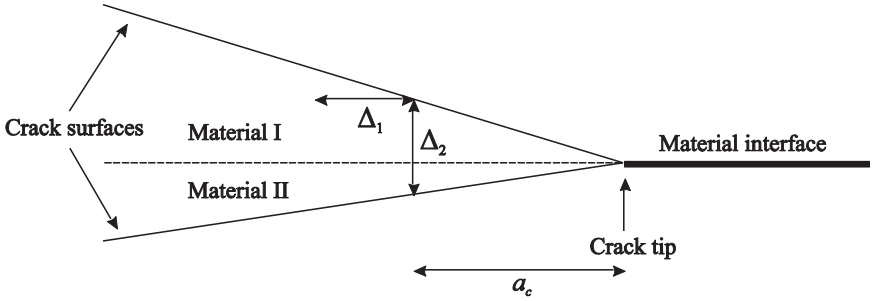

Fig. 4. Horizontal and vertical displacements at the distance a_c behind the crack tip.

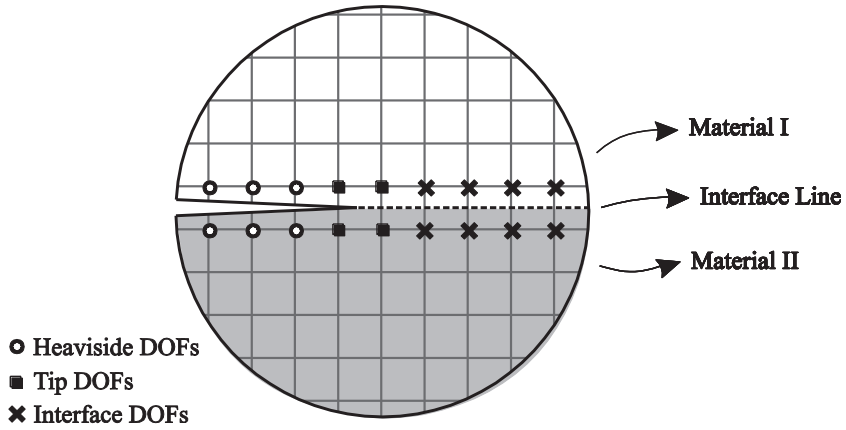

Fig. 5. Selecting the three types of enriched nodes for an interface crack problem.

5. Numerical implementation

5.1. Spatial discretization with XFEM

XFEM modeling of interface crack consists of three parts of capturing the crack tip singularity, modeling the strong discontinuity across the crack surfaces and simulating the weak discontinuity (discontinuous strain field) across the material interface. Therefore, approximation of the displacement field is enhanced by three enrichment functions:

$$\mathbf{u}(\mathbf{x}) = \sum_{i=1}^{n} \underbrace{N_i(\mathbf{x})}_{\Phi_i^{\mathrm{d}}} \mathbf{d}_i + \sum_{j=1}^{m} \underbrace{N_j(\mathbf{x}) H(\mathbf{x})}_{\Phi_j^{\mathrm{a}}} \mathbf{a}_j + \sum_{l=1}^{p} \underbrace{N_l(\mathbf{x}) \left(\sum_t F_t(\mathbf{x}) \right)}_{\Phi_l^{\mathrm{b}}} \mathbf{b}_l + \sum_{k=1}^{q} \underbrace{N_k(\mathbf{x}) \chi_k(\mathbf{x})}_{\Phi_k^{\mathrm{c}}} \mathbf{c}_k \tag{26}$$

where n, m, p and q are the number of conventional, crack surface, crack tip, and interface nodes, respectively (see Fig. 5). $\mathbf{d}_i$ is the vector of regular degrees of freedom. In addition, $\mathbf{a}_j$, $\mathbf{b}_l$ and $\mathbf{c}_k$ are the vectors of additional degrees of freedom associated with the crack surface, crack tip, and material interface, respectively. $H(\mathbf{x})$ and $\chi_k(\mathbf{x})$ are the Heaviside and weak discontinuity enrichment functions, respectively. More details about these functions are available in Refs. [24,54]. $F_t(\mathbf{x})$ is the oscillatory enrichment function for the interface crack tip between two orthotropic materials [16],

$$F(r,\theta) = \begin{Bmatrix} e^{-\varepsilon\theta_l}\cos(\varepsilon ln(r_l) + \frac{\theta_l}{2})\sqrt{r_l} & e^{-\varepsilon\theta_l}\sin(\varepsilon ln(r_l) + \frac{\theta_l}{2})\sqrt{r_l} \\ e^{\varepsilon\theta_l}\cos(\varepsilon ln(r_l) - \frac{\theta_l}{2})\sqrt{r_l} & e^{\varepsilon\theta_l}\cos(\varepsilon ln(r_l) - \frac{\theta_l}{2})\sqrt{r_l} \\ e^{-\varepsilon\theta_s}\cos(\varepsilon ln(r_s) + \frac{\theta_s}{2})\sqrt{r_s} & e^{-\varepsilon\theta_s}\sin(\varepsilon ln(r_s) + \frac{\theta_s}{2})\sqrt{r_s} \\ e^{\varepsilon\theta_s}\cos(\varepsilon ln(r_s) - \frac{\theta_s}{2})\sqrt{r_s} & e^{\varepsilon\theta_s}\cos(\varepsilon ln(r_s) - \frac{\theta_s}{2})\sqrt{r_s} \end{Bmatrix} \tag{27}$$

where r_l, r_s, θ_l and θ_s are determined from Eqs. (A.10)–(A.12) of Appendix A. It should be noted that Eqs. (A.10)-(A.18) and so the enrichment function (27) depend on the crack velocity. Esna Ashari and Mohammadi [16] studied the effects of two cases of crack tip enrichment functions (the oscillatory crack tip enrichment functions and the original isotropic crack tip enrichment functions) and concluded that using the original isotropic crack tip enrichment functions could result in significant errors in computing the stress intensity factors in orthotropic bi-material problems.

It should be noted that although the ramp enrichment function has not been used for the elements in the vicinity of the tip element, a smooth transition has been considered in order to avoid sharp changes between the tip element and its neighboring elements. This is achieved by enriching some nodes of the neighboring elements, as similarly performed by a number of references with reportedly acceptable results [16,21,24,40,41,55]. As a result, in the neighboring elements of a tip element, standard shape functions vary from a nonzero value on one side of the element to zero on the other side. Therefore, multiplying standard shape functions by oscillatory enrichment functions introduces new functions which not only possess the desired behavior but also vanish smoothly in the outer edges of the neighboring elements.

5.2. Discretization of momentum equation

The discretized weak form of the governing Eq. (1) based on the XFEM approximation at time n can be written as (neglecting the effects of damping),

$$\mathbf{M}\ddot{\mathbf{u}}_{\mathrm{n}} + \mathbf{K}\mathbf{u}_{\mathrm{n}} = \mathbf{f}_{\mathrm{n}} \tag{28}$$

where $\mathbf{u}_{\mathrm{n}}$ is composed of the standard and enriched vectors of nodal degrees of freedom:

$$\mathbf{u}_{\mathrm{n}} = \{\mathbf{d} \quad \mathbf{a} \quad \mathbf{b} \quad \mathbf{c}\}^{\mathrm{T}}$$

$\mathbf{d}$: vector of standard nodal degrees of freedom

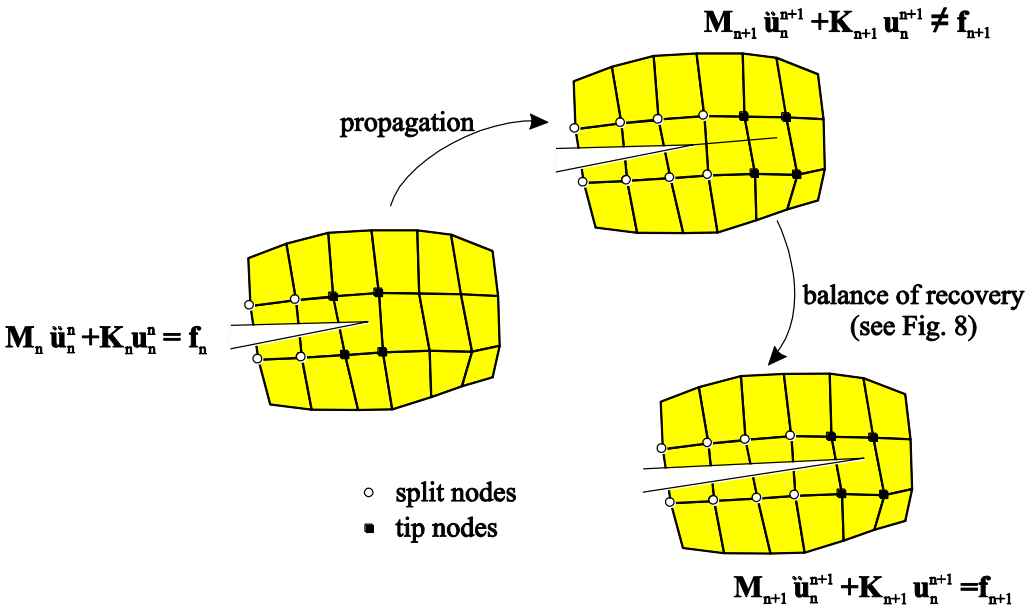

Fig. 6. Schematic procedure of balance of recovery.

$$\begin{aligned}&\mathbf{a}\ :\ \text{vector of Heaviside enrichment degrees of freedom}\\&\mathbf{b}\ :\ \text{vector of oscillatory crack tip enrichment degrees of freedom}\\&\mathbf{c}\ :\ \text{vector of weak discontinuity enrichment degrees of freedom}\end{aligned}\tag{29}$$

Also, $\mathbf{f}_n$ is the external force vector, and $\mathbf{M}$ and $\mathbf{K}$ are the mass and stiffness matrices, respectively. For an element e, they can be computed from,

$$\mathbf{M}_{ij}^{rs}=\int_{\Omega^e}\rho\left(\Phi_i^r\right)\left(\Phi_j^s\right)d\Omega\,(r,s=d,a,b,c)\tag{30}$$

$$\mathbf{K}_{ij}^{rs}=\int_{\Omega^e}\left(\mathbf{B}_i^r\right)^{\mathrm{T}}\mathbf{C}\left(\mathbf{B}_j^s\right)d\Omega\,(r,s=d,a,b,c)\tag{31}$$

$$\mathbf{f}_i^r=\int_{\partial\Omega\cap\partial\Omega}\left(\Phi_i^r\right)\mathbf{T}d\Gamma\,(r=d,a,b,c)\tag{32}$$

where $\mathbf{T}$ is the vector of external traction. Φ represents the standard and enriched shape functions (see Eq. (26)) and $\mathbf{B}$ is the matrix of derivatives of shape functions Φ, all comprehensively defined in Ref. [54]. The sub-triangulation technique is used to integrate Eq. (31) (more details are available in the work by Esna Ashari and Mohammadi [16]).

5.3. Time integration method

Different time integration methods are available for solving the system of Eq. (28). In problems where the external loading is dynamic and the crack does not propagate, the Newmark time integration method remains sufficiently accurate, whereas in crack propagation problems the Newmark method results in numerical oscillations as the stiffness matrix varies in two consecutive time steps. These oscillations increase over time and may even lead to an unstable response. To overcome this difficulty in the present study, the time discontinuous finite element method is adopted [43,44]. This method, based on the weighted residual form proposed by Zienkiewicz [56], uses the finite element method approximation in time instead of the finite difference approach. For a velocity based formulation, a linear velocity approximation is adopted,

$$\mathbf{v}=\dot{\mathbf{u}}=\sum_{i=n,n+1}N_i(t)\mathbf{v}_i\tag{33}$$

where N_i is the shape function of 2-node one-dimensional element (time span).

According to the time discontinuous finite element method, the Heaviside enrichment function is added to the velocity approximation $\mathbf{v}$ in the time span $I_n=]t_n,\ t_{n+1}[$ [44]:

$$\mathbf{v}(t)=\underbrace{\mathbf{v}_n^{\mathrm{s}}N_n(t)+\mathbf{v}_{n+1}^{\mathrm{s}}N_{n+1}(t)}_{\mathbf{v}^{\mathrm{s}}(t)}+\underbrace{\mathbf{v}_n^{\mathrm{e}}N_n(t)\mathrm{H}(t-t_n)}_{\mathbf{v}^{\mathrm{e}}(t)}\tag{34}$$

where $\mathbf{v}_n^{\mathrm{s}}$ and $\mathbf{v}_{n+1}^{\mathrm{s}}$ are the vectors of standard velocity degrees of freedom and $\mathbf{v}_n^{\mathrm{e}}$ is the vector of additional velocity degrees of freedom.

The third term in Eq. (34) ensures the velocity discontinuity before and after each time level:

$$\left.\begin{aligned}\mathbf{v}_n^+&=\mathbf{v}_n^{\mathrm{s}}+\mathbf{v}_n^{\mathrm{e}}\\\mathbf{v}_n^-&=\mathbf{v}_n^{\mathrm{s}}\end{aligned}\right\}\rightarrow\mathbf{v}_n^+-\mathbf{v}_n^-=\mathbf{v}_n^{\mathrm{e}}\tag{35}$$

Having known the variables $\mathbf{u}_n^{\mathrm{s}}$, $\mathbf{v}_n^{\mathrm{s}}$, $\mathbf{u}_n^{\mathrm{e}}$, $\mathbf{v}_{n-1}^{\mathrm{e}}$, the following system of equations can be solved for unknowns $\mathbf{v}_n^+,\mathbf{v}_{n+1}^-$,

$$\begin{bmatrix}\mathbf{M}-\frac{\Delta t^2}{12}\mathbf{K} & -\frac{\Delta t^2}{12}\mathbf{K}\\ +\frac{\Delta t^2}{3}\mathbf{K} & \mathbf{M}-\frac{\Delta t^2}{6}\mathbf{K}\end{bmatrix}\begin{bmatrix}\mathbf{v}_n^+\\\mathbf{v}_{n+1}^-\end{bmatrix}=\begin{bmatrix}\mathbf{F}_1-\mathbf{F}_2+\mathbf{M}\mathbf{v}_n^-\\\mathbf{F}_1+\mathbf{F}_2+\mathbf{M}\mathbf{v}_n^--\mathbf{K}\mathbf{u}_n^-\Delta t\end{bmatrix}\tag{36}$$

where $\mathbf{F_1}$ and $\mathbf{F_2}$ are defined in terms of the external load,

$$\mathbf{F}_1=\frac{\Delta t}{3}\mathbf{f}_n+\frac{\Delta t}{6}\mathbf{f}_{n+1}\tag{37}$$

$$\mathbf{F}_2=\frac{\Delta t}{6}\mathbf{f}_n+\frac{\Delta t}{3}\mathbf{f}_{n+1}\tag{38}$$

Finally, continuous displacement and acceleration fields can be determined from,

$$\mathbf{u}_{n+1}^+=\mathbf{u}_{n+1}^-=\mathbf{u}_n+\frac{\Delta t}{2}\left(\mathbf{v}_{n+1}^-+\mathbf{v}_n^+\right)\tag{39}$$

$$\mathbf{a}_{n+1}=\frac{\left(\mathbf{v}_{n+1}^--\mathbf{v}_n^+\right)}{\Delta t}\tag{40}$$

Based on Eqs. (36)–(40), while the displacement remains continuous in each time level, the velocity becomes discontinuous. This discontinuous velocity allows for a more stable simulation of crack propagation, especially at later stages of crack propagation when the crack speed becomes close to the shear wave speed.

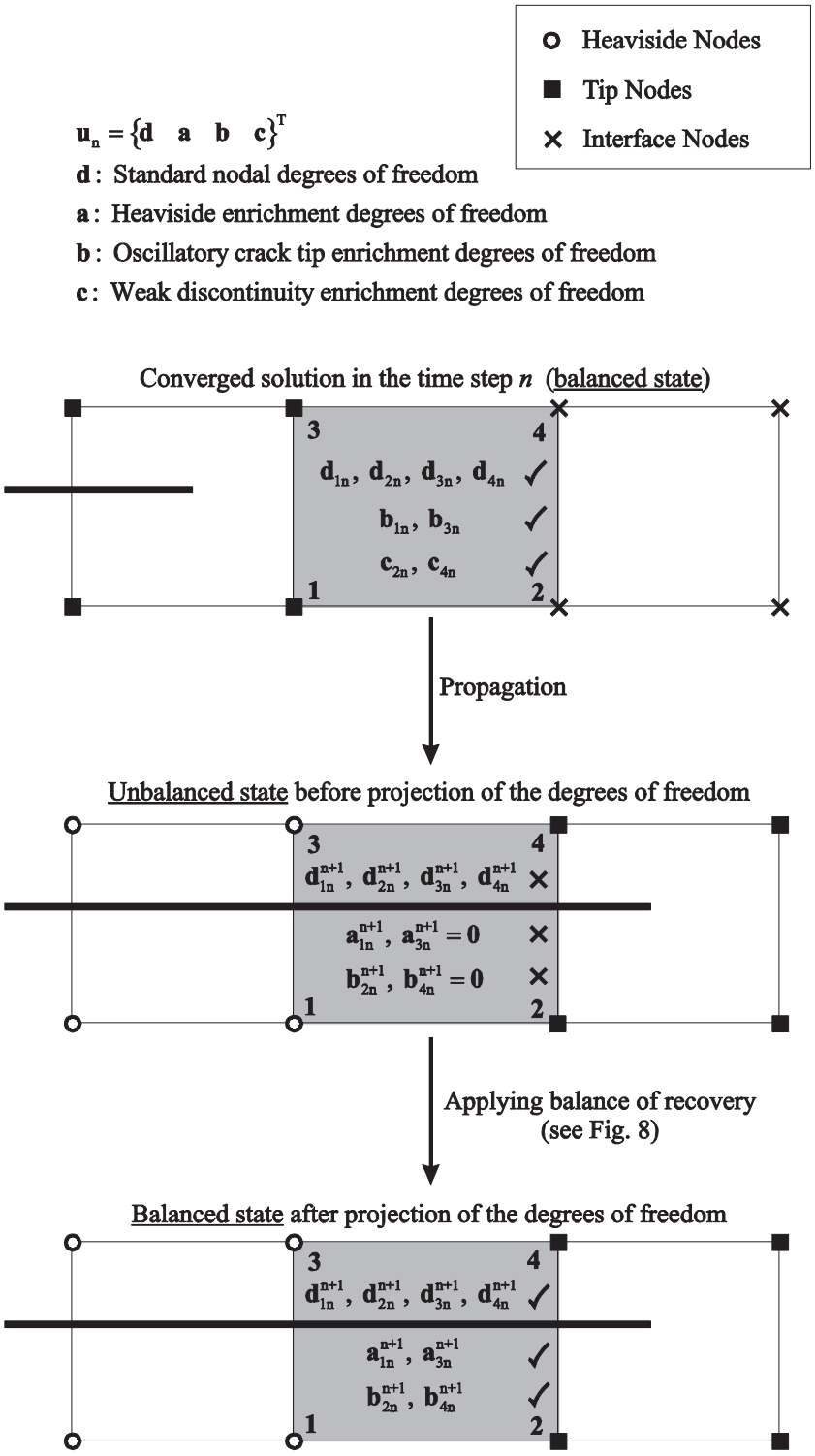

Fig. 7. Detailed procedure for projecting the degrees of freedom of the nth time step on the new configuration.

5.4. Iterative algorithm for determination of crack velocity

According to Eq. (19), both the energy release rate G and the critical dynamic fracture energy release rate G_c depend on the crack velocity at each time step, and the crack velocity is calculated in such a way that $G(V)$ becomes equal to $G_c(V)$; $G(V) - G_c(V) = 0$. The secant iterative method is employed here to solve this nonlinear equation. At the beginning of each time step, an initial value is selected for the crack velocity, and then it is modified by

$$V_n^{k+1} = V_n^k + \frac{(V_n^{k-1} - V_n^k) f(V_n^k)}{f(V_n^k) - f(V_n^{k-1})} \tag{41}$$

with

$$f(V_n) = G(V_n) - G_c(V_n) \tag{42}$$

where n is the number of time steps, and k is the iteration number at each time step. At each time step, the secant iterative algorithm requires

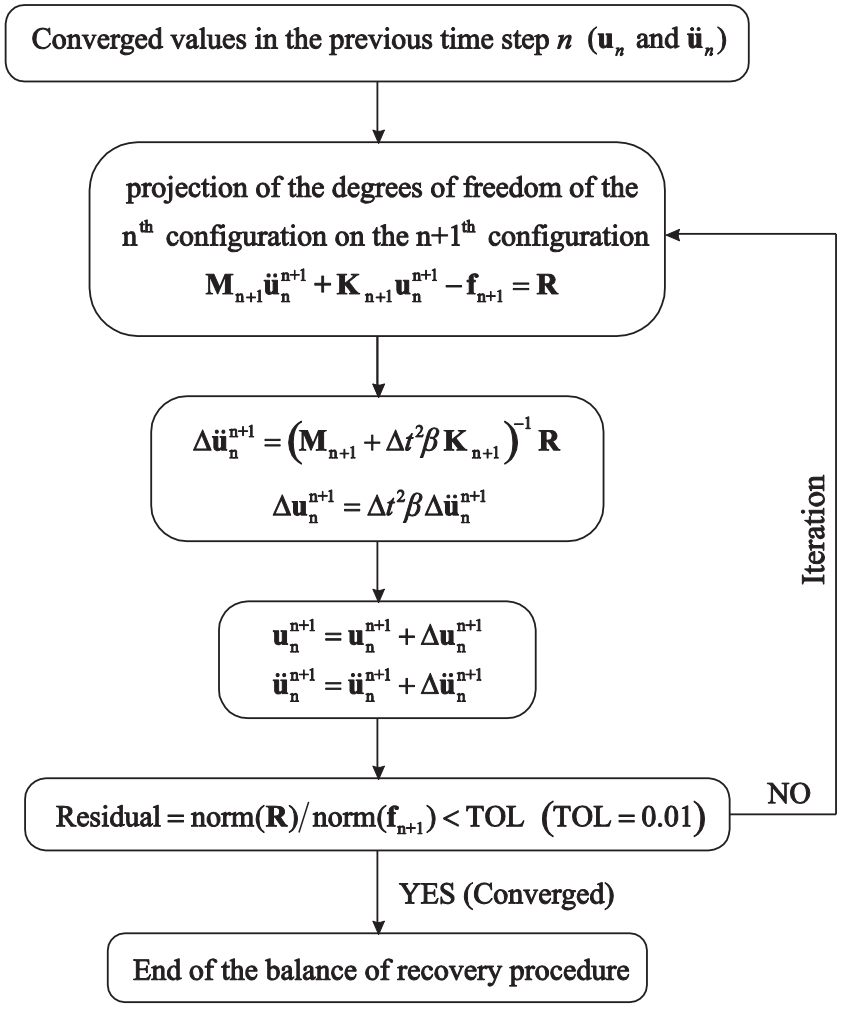

Fig. 8. Iterative algorithm of balance of recovery method.

two initial guesses for the crack velocity: the crack velocity in the previous step and an arbitrary guess are the two initial estimations. If the crack velocity does not satisfy Eq. (41), the crack position and other fields (displacement, velocity, acceleration, etc.) are returned to the initial values of the time step, and a new guess is then made using Eq. (42). Iteration continues until the following convergence criterion is satisfied:

$$\left|G(V_n) - G_c(V_n)\right| / G_c^* < \text{TOL} \tag{43}$$

In this paper, TOL is considered 2% and four iterations, on average, are needed for each time step.

5.5. Balance of recovery method

In an XFEM formulation, due to the crack propagation and the movement of the crack tip position, new degrees of freedom should be added to the nodes. These degrees of freedom have null values before solving Eq. (28), which leads to an invalid geometry for crack [57] (see Figs. 6 and 7). In other words, by projecting the degrees of freedom of the nth time step on the new configuration ($n+1$th configuration), out of balance forces $\mathbf{R}$ are generated in the equilibrium equation, which results in numerical oscillations:

$$\mathbf{M}_n\ddot{\mathbf{u}}_n + \mathbf{K}_n\mathbf{u}_n = \mathbf{f}_n \tag{44}$$

$$\mathbf{M}_{n+1}\ddot{\mathbf{u}}_n^{n+1} + \mathbf{K}_{n+1}\mathbf{u}_n^{n+1} - \mathbf{f}_{n+1} = \mathbf{R} \neq 0 \tag{45}$$

where $\mathbf{u}_n^{n+1}$ and $\ddot{\mathbf{u}}_n^{n+1}$ are the projection of the degrees of freedom of the nth configuration on the $n+1$th configuration. Different approaches are available for removing the unbalanced forces in crack propagation problems. One approach is the load relaxation phase analysis, suitable in material nonlinearity cases [31]. The method has a procedure for data transfer of the history variables from old crack geometry to new crack geometry, and the traction forces are gradually released from the extended crack surface using an iterative algorithm. Another approach, the balance of recovery method [58], is applied for linear elastic fracture analysis to iteratively remove the unbalancing forces in Eq. (45). Accordingly, the unbalanced state of the system (Eq. (45)) is solved after projection of the degrees of freedom and before solving the system of equations for time $n+1$, leading to the removal of the residual (45) (see Fig. 8). It should be noted that all variables in Eq. (45) are nodal variables ($\mathbf{u}_n^{n+1}, \ddot{\mathbf{u}}_n^{n+1}$). Therefore, no data transfer procedure is required from Gauss points to nodal points, and vice versa. Figs. 6–8 show the detailed procedure of the adopted balance of recovery method.

With a simple assumption for $\Delta\mathbf{u}_n^{n+1}$,

$$\Delta\mathbf{u}_n^{n+1} = \Delta t^2\beta\Delta\ddot{\mathbf{u}}_n^{n+1} \tag{46}$$

and solving Eq. (45) for $\Delta\ddot{\mathbf{u}}_n^{n+1}$,

$$\Delta\ddot{\mathbf{u}}_n^{n+1} = \left(\mathbf{M}_{n+1} + \Delta t^2\beta\mathbf{K}_{n+1}\right)^{-1}\mathbf{R} \tag{47}$$

The modified values of displacement and acceleration are calculated

$$\mathbf{u}_n^{n+1} = \mathbf{u}_n^{n+1} + \Delta\mathbf{u}_n^{n+1} \tag{48}$$

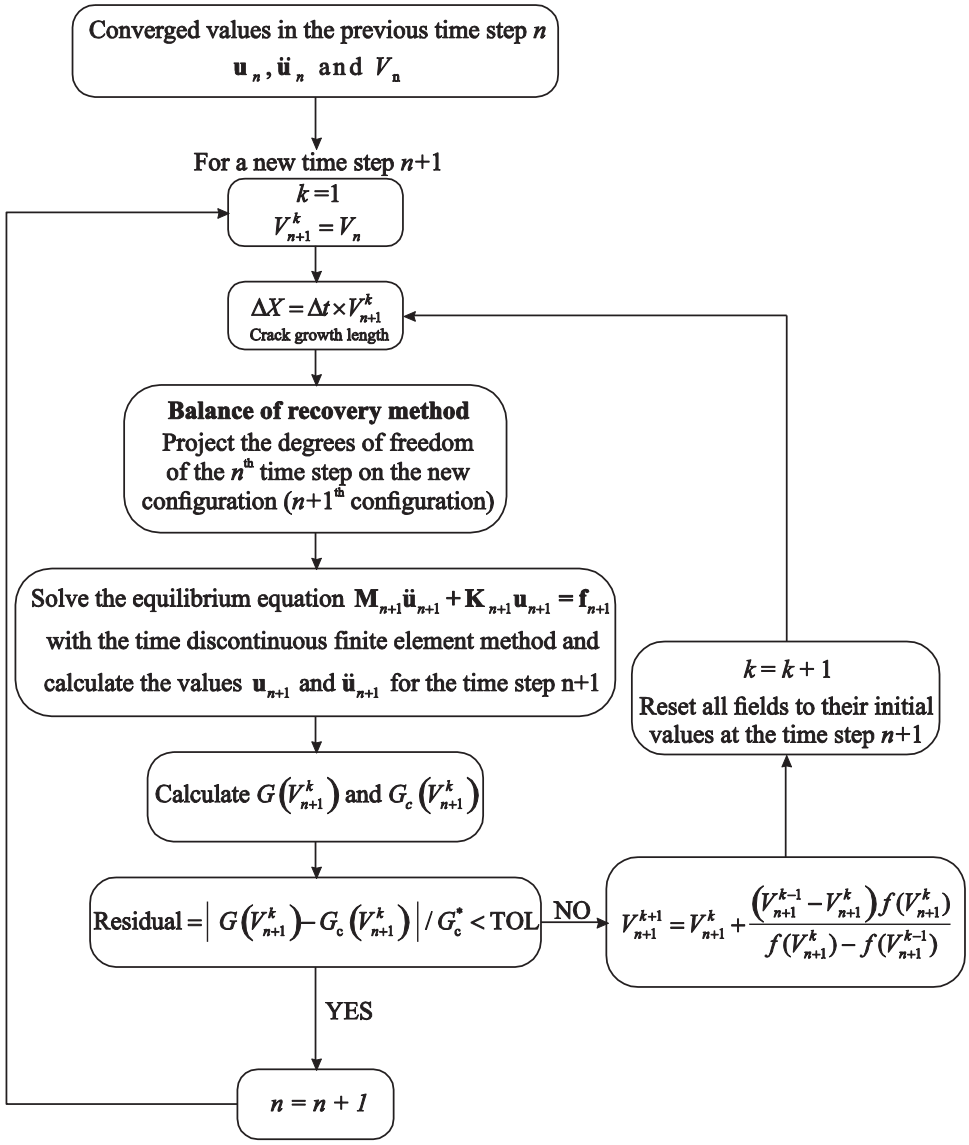

Fig. 9. General algorithm of dynamic interface crack growth.

$$\ddot{\mathbf{u}}_{\mathrm{n}}^{\mathrm{n+1}} = \ddot{\mathbf{u}}_{\mathrm{n}}^{\mathrm{n+1}} + \Delta\ddot{\mathbf{u}}_{\mathrm{n}}^{\mathrm{n+1}} \tag{49}$$

In order to accurately predict the fracture parameters in this study, both the balance of recovery method and the time discontinuous finite element integration algorithm are employed, considerably stabilizing the otherwise oscillating solution, as will be discussed in the numerical examples.

The general procedure of dynamic interface crack growth is presented in Fig. 9. This algorithm is applied for the numerical simulations in Section 6.

6. Numerical results

6.1. Dynamic crack growth in an infinite isotropic plate

In order to verify the proposed method for calculating the interaction integral (*M*-integral), the time discontinuous finite element method and the balance of recovery method, an infinite homogeneous plate with a semi-infinite crack [40,44,59], for which the analytical solution is available, is simulated. An isotropic plate is assumed to be under a tensile loading on its top edge, with plane strain condition, as shown in Fig. 10.

Table 1
Material properties of the problem.

Parameter	Value
E(GPa)	210
ν	0.3
ρ(kg/m^3)	8000

The material properties are listed in Table 1. In this example, all results related to the dynamic stress intensity factor are normalized by $\boldsymbol{\sigma}\sqrt{\mathrm{H}}$.

The external traction applied on the top edge is:

$$\boldsymbol{\sigma}(t) = \begin{cases} t/(0.2t_c) & 0 \le t \le 0.2t_c \\ 1 & 0.2t_c \ge t \end{cases} \tag{50}$$

where t_c is the time that the longitudinal wave travels half the height of the plate, and is equal to:

$$t_c = \frac{h}{c_L} \tag{51}$$

where c_L is the longitudinal wave speed and is equal to 5944 m/s [59].

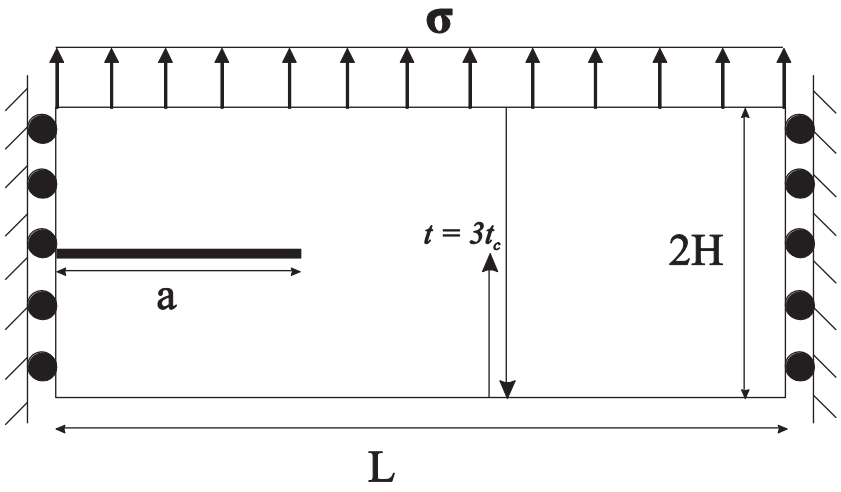

Fig. 10. Geometry and boundary conditions of the problem.

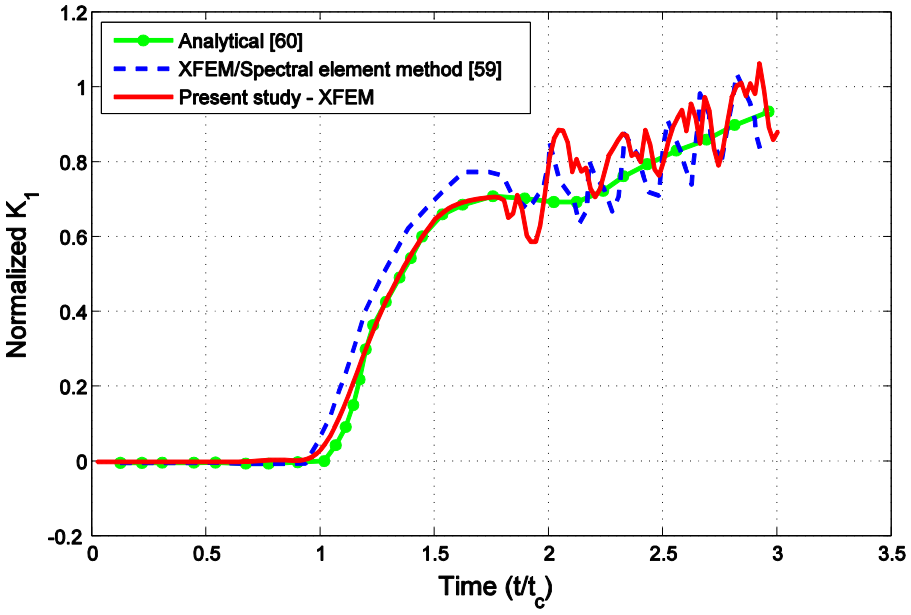

Fig. 11. Comparison of dynamic stress intensity factor for a moving crack in the infinite isotropic plate.

In this problem, the crack tip velocity is assumed to be known, and the crack propagates with the velocity reported by Liu et al. [59]:

$$V = \begin{cases} 0 & t \le 1.5t_c \\ V_0 \sin\left(\frac{(t-1.5t_c)\pi}{1.4t_c}\right) & 1.5t_c \le t \le 2.2t_c \\ V_0 & t \ge 2.2t_c \end{cases} \tag{52}$$

where V_0 is equal to 1500 m/s. The analytical solution of the problem was presented by Freund [60],

$$K(V,t) = \begin{cases} 0 \\ \frac{2\sigma(t)(1-V/c_R)}{1-\upsilon}\sqrt{\frac{c_L(t-t_c)(1-2\upsilon)}{\pi(1-V/c_L)}} \end{cases} \tag{53}$$

This analytical solution is associated with an infinite plate; therefore, the numerical simulation is carried out only until $t=3t_c$, i.e. when the reflected longitudinal wave from the bottom boundary reaches the crack tip (see Fig. 10).

Simulation is performed with a uniform 40×80 finite element mesh, the domain integral of 0.5 mm, the time discontinuous finite element method with a time step of $\Delta t = 0.2t_c$, and the balance of recovery method. The calculated dynamic stress intensity factor is presented in Fig. 11 and is compared with those obtained by Liu et al. [59], which utilized the spectral element method. A good agreement is clearly observed between the analytical and numerical results, which confirms the validity of adopted techniques, including the interaction integral method with the auxiliary fields.

To evaluate the effect of time integration method on the stability of the solution, the problem is also solved by the Newmark method. The results of dynamic stress intensity factor are given in Fig. 12, which shows that the time discontinuous finite element method considerably reduces the existing oscillations in the numerical solution. It is also observed that, as long as the crack is stationary, the results of the Newmark method are in agreement with those obtained by the analytical and the time discontinuous finite element methods; however, when the crack propagates, oscillations appear and increase. In a real analysis, where the crack tip velocity is not an input data of the problem, similar to what comes in the next example, the increasing numerical oscillations over the time make the prediction of quantities such as crack tip velocity, energy release rate and dynamic stress intensity factor practically impossible. Hence, adopting a stable numerical solution is an essential requirement for accurate prediction of crack tip velocity.

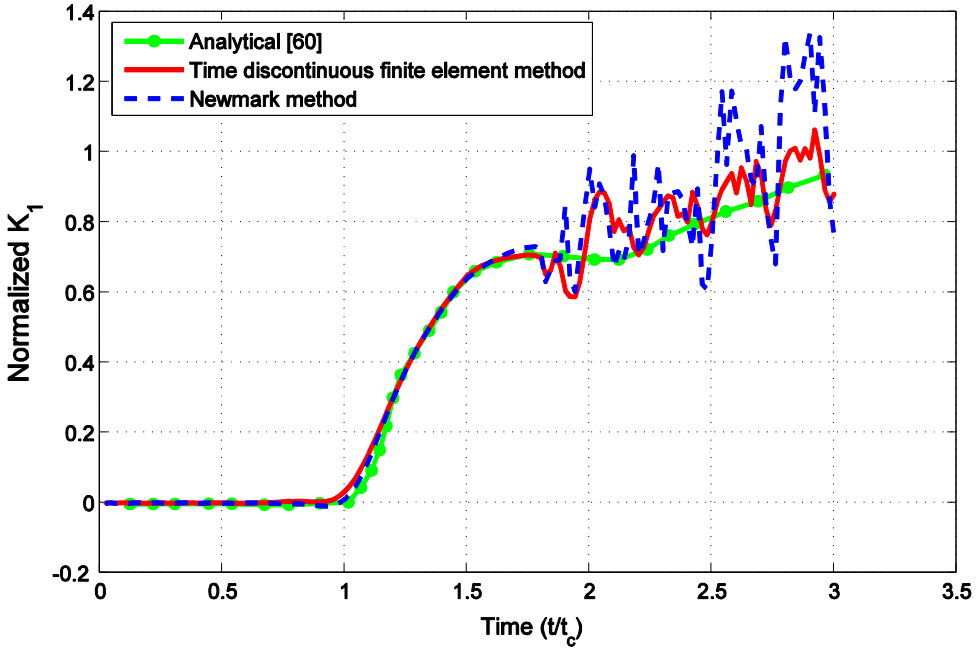

Fig. 12. Effect of time integration method in the stability of the solution.

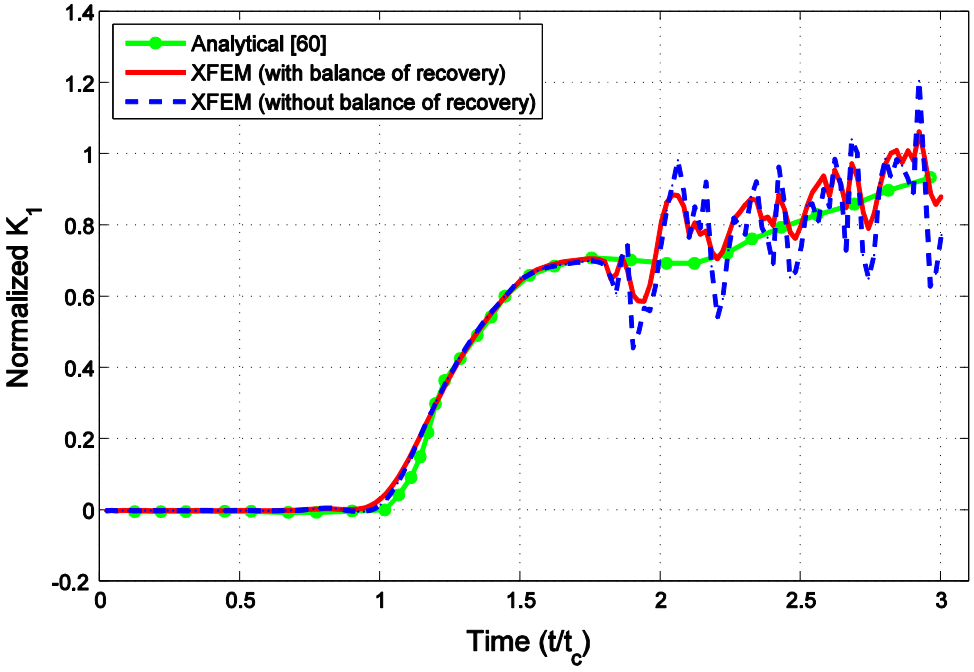

Fig. 13. The effect of balance of recovery method on the stability of the results.

Changing the standard finite element to the enriched element in the extended finite element (due to crack propagation in that element) and adding new degrees of freedom to elements lead to numerical oscillations and out of balance force at the beginning of every time step. To illustrate the effect of the balance of recovery method, the problem is solved again by neglecting this algorithm, as depicted in Fig. 13. Clearly, this algorithm has a considerable impact on reducing the numerical oscillations and stabilizing the solution.

The results obtained from this example show that the combined use of the balance of recovery method and the time discontinuous finite element method substantially improves the stability of dynamic crack propagation analysis. The next example extends this stable procedure to a problem in which the crack propagation velocity is not known a priori.

6.2. *Dynamic crack growth along a PMMA-steel bi-material interface*

After evaluating the dynamic crack growth in a homogeneous body, one of the main dynamic interface crack propagation experiments is numerically analyzed here. This experiment was carried out by Lambros and Rosakis [53] and includes an impact loading on a bi-material composite consisting of steel and polymethylmethacrylate (PMMA). The geometry and impact loading are shown in Fig. 14. The mechanical properties of each layer are presented in Table 2, with an oscillating index of $\epsilon = 0.1037$. The fracture toughness for crack propagation is

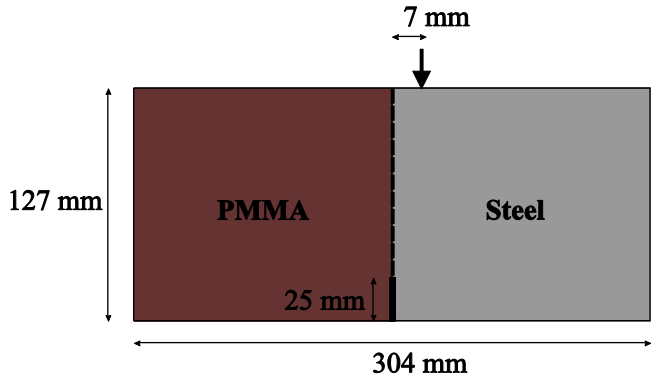

Fig. 14. Geometry and boundary conditions.

Table 2
Material properties of the problem.

Parameter	Value	
	steel	PMMA
E(GPa)	208	3.24
υ	0.30	0.35
ρ(kg/m^3)	7830	1190

120N/m. This plane stress problem is simulated with a 45 × 150 finite element mesh, domain integral of 5 mm, time discontinuous finite element method with a time step of 1.5 μs, and the balance of recovery method.

By using High-speed photography, Lambros and Rosakis were able to accurately measure the energy release rate, phase angle, and crack tip velocity during their experiment [53]. Also, Nakamura et al. [47] numerically analyzed this problem, which will be used for comparison.

Here, the numerical simulation is performed in two stages. In the first stage, the crack tip velocity is assumed to be known, and the crack propagates with the velocity reported by Lambros and Rosakis [53]. The input velocity history is shown in Fig. 15. In the second stage, the crack tip velocity is not taken as an input data and instead, is calculated using the fracture criteria presented in Section 4 (Eqs. (19) and (25)) and the iterative algorithm described in Section 5.4.

The energy release rate obtained from the numerical analysis along with the reference values [53] are presented in Fig. 16. First, an attempt is made to investigate the effect of oscillatory crack tip enrichment functions. A good agreement is observed between the reference experimental values and the results obtained with XFEM formulation considering the oscillatory tip enrichments. It is noted that in the cases of XFEM with standard crack tip enrichment functions and XFEM without enrichments, the highly oscillatory results gradually diverge from the reference solution and become unstable. Fig. 16 shows that before the crack growth, ignoring the oscillatory crack tip enrichments does not significantly affect the results. After the crack growth, however, it leads to significant spurious oscillations and generates inaccurate values. This clearly emphasizes the importance of the oscillatory crack tip enrichment functions in the present dynamic crack propagation analysis.

In addition, Fig. 17 shows the stress distribution near the crack tip (distance from crack tip = 0.01 mm) in the left material for the following three cases: 1. the oscillatory crack tip enrichments, 2. the standard crack tip enrichments, and 3. ignoring the crack tip enrichments. In this figure, the stress is plotted for the crack length of 26.7 mm (time = 85 μs and the crack tip velocity = 360 m/s). It is observed that the crack tip singularity is accurately captured by the oscillatory crack tip enrichments. Standard crack tip enrichments generate far lower level of singular stress field. No crack tip singularity is obtained if crack tip enrichments are ignored.

Table 3
Three unstructured meshes.

Unstructured mesh	Number of nodes and elements	Size of crack tip element
Coarse	6182 nodes, 6028 elements	$h \approx 2.9$ mm
Medium	11,690 nodes, 11,420 elements	$h \approx 1.8$ mm
Fine	18,402 nodes, 18,054 elements	$h \approx 1.4$ mm

In order to examine the convergence of the solution, the problem is analyzed by a set of different structured meshes (25 × 100, 45 × 150, 75 × 200, 100 × 250, 200 × 400, 300 × 600, and 400 × 800 elements) and the energy release rates are presented in Fig. 18. Clearly, all meshes, except the very coarse mesh, provide similar and acceptable results. Also, it is expectedly observed that the energy release rate converges to the solution by the finest mesh as the mesh becomes finer.

To demonstrate the effect of mesh type (structured and unstructured meshes), the analysis is further extended based on three new unstructured meshes (see Table 3). Fig. 19 shows a typical unstructured mesh around the crack tip. Time history of energy release rate for different meshes (150 × 45 structured mesh, 200 × 75 structured mesh, 250 × 100 structured mesh, coarse unstructured mesh, medium unstructured mesh, and fine unstructured mesh) are compared in Fig. 20. It is clearly observed that all meshes provide similar and acceptable results.

Fig. 21 shows the effect of the time integration method on the stability of the results. It is clearly observed that the time discontinuous finite element method significantly reduces the numerical oscillations in comparison with the Newmark method. Again, it is observed that the Newmark method performs accurately before crack propagation, while it causes substantial oscillations in the numerical results after crack propagation. In fact, in this case, when the crack tip velocity is determined during the numerical analysis and based on the criterion presented in Section 4, the oscillations lead to divergence of the solution and instability. The reason can be attributed to the fact that if the energy release rate (G) has large oscillations during the solution process, Eq. (19) cannot be solved and, therefore, no value is obtained for the crack tip velocity.

In the second part, the crack tip velocity is calculated using the criterion presented in Section 4 (Eqs. (19) and (25)) and the iterative algorithm described in Section 5.4. For this purpose, the constants C and n in Eq. (25) are considered 0.04 and 0.08, respectively.

The crack tip velocity, depicted in Fig. 22, shows a good agreement between the experimental values and the obtained numerical results (with the oscillatory tip enrichment functions). In contrast to the fracture criterion proposed by Nakamura et al. [47] (Eq. (21)), which is not based on experimental tests and the solution diverges at time 86μs, the fracture criterion proposed by Kavaturu and Shukla [52] (Eq. (25)) is very close to the experimental results and the solution converges in the whole time domain. In addition, Fig. 22 illustrates that neglecting the effects of the oscillatory crack tip enrichments decreases the accuracy of the solution in determining the crack tip velocity.

The resulting energy release rate is shown in Fig. 23 along with the reference values [53]. It can be observed that there is no difference between the case that the crack tip velocity is calculated using Eqs. (19) and (25) (blue solid line in Fig. 23) and the case that the crack propagates with the experimental velocity reported by Lambros and Rosakis [53] (green dash line in Fig. 23). Also, there is a good agreement between the experimental results and numerical predictions by considering the crack tip enrichments. Furthermore, Fig. 23 shows that the results of ignoring the tip enrichments substantially increases the numerical oscillations and reduces the accuracy compared with the experimental values.

6.3. Dynamic crack growth along a polymer composite–Homalite interface

This example addresses the dynamic interface crack growth in orthotropic bi-materials, as it frequently occurs in various engineering ap-

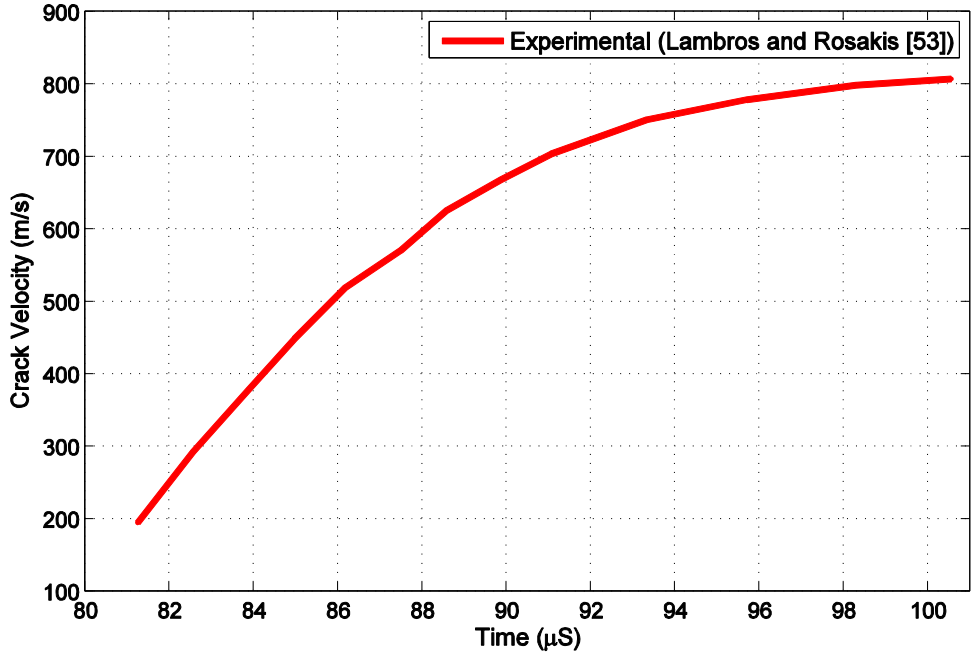

Fig. 15. The crack velocity recorded in the experiment by Lambros and Rosakis [53].

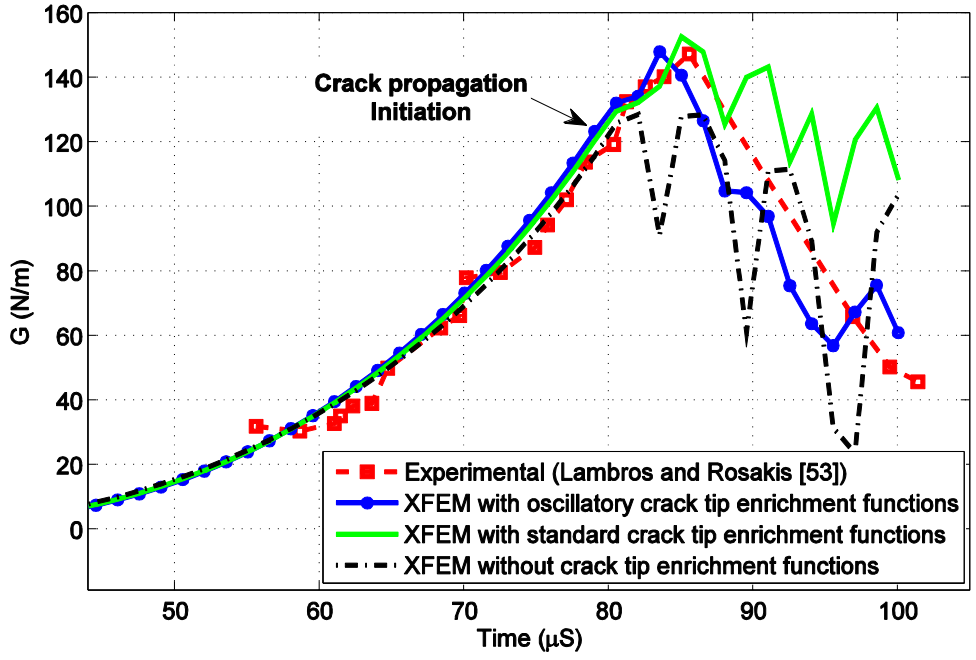

Fig. 16. Time history of energy release rate in the case that the crack tip velocity is an input data of the problem.

plications. The material properties are presented in Table 4, where $E_{\parallel}$ is the Young modulus in the direction of the fibers, and $E_{\perp}$ is the Young modulus in the direction perpendicular to the fibers. Eqs. (19) and (25) are used with constants C= 0.01 and n= 0.08 to determine the crack tip velocity. One layer is isotropic, and the other one is orthotropic. Geometry and dimensions of the model and the applied loading are presented in Fig. 24.

The specimen has the thickness of 10 mm and the problem is simulated under the plane stress condition. The dynamic analysis is performed with a 45 × 150 finite element mesh and the domain integral of 5 mm. The problem is solved with six different time steps (Δt = 1.5, 1, 0.5, 0.2, 0.15 and 0.1 μs) to evaluate the sensitivity of the results to the time steps. Results of energy release rate and crack length for different time steps are presented in Figs. 25 and 26, which are nearly similar results. Also, Figs. 25 and 26 show that the convergence in time is obtained by decreasing the time step.

Figs. 27 and 28 show the effect of the oscillatory crack tip enrichments on the energy release rate and crack length. Clearly, ignoring the enrichment functions leads to large oscillations and subsequent instability.

Fig. 29 shows the stress distribution near the crack tip in the top material for two cases: (1) using the oscillatory crack tip enrichments and (2) ignoring the crack tip enrichments. In this graph, the stress is plotted for the crack lengths of 30.5 mm and 40.8 mm. Since the crack tip velocity is different for the two cases, the stress near the crack tip for case 1 is reported at times 61 and 65 μs, while it is reported at times 73 and

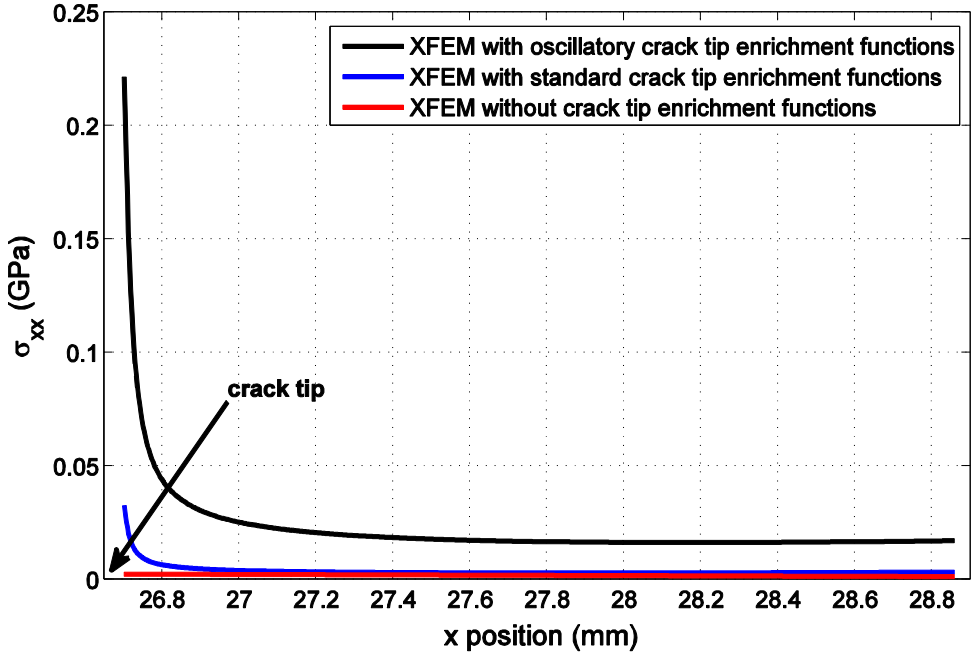

Fig. 17. Effect of crack tip enrichment functions on the stress distribution near the crack tip.

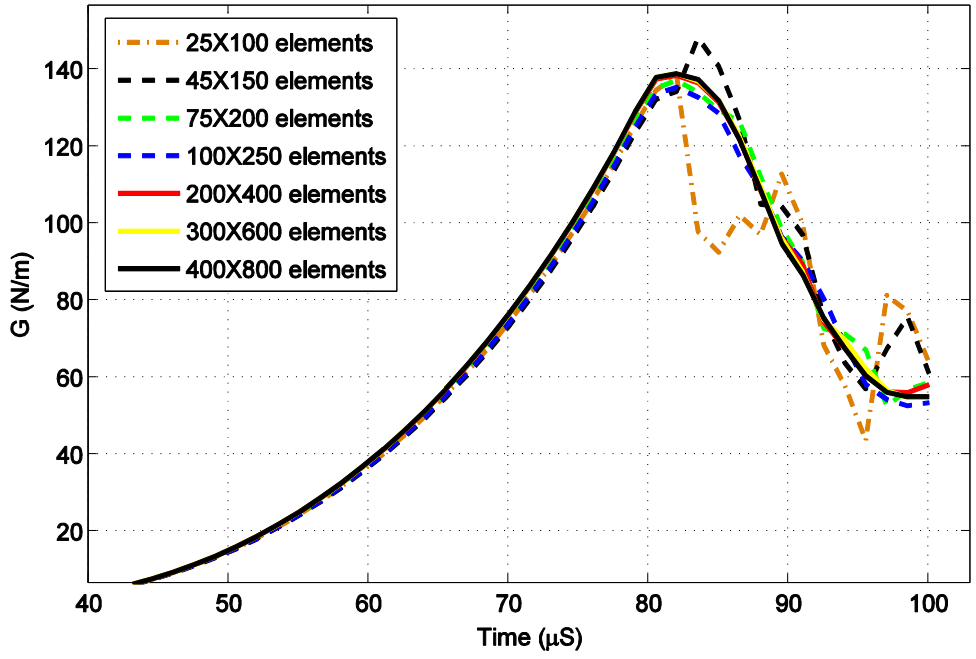

Fig. 18. Effect of mesh size on the time history of energy release rate.

78μs for case 2 (see Fig. 28). It is observed that the crack tip singularity is not obtained for the case of ignoring the crack tip enrichments.

Finally, in Fig. 30, the stress contours (σ_{yy}) are plotted at different times to show the stress wave propagation in the body. It can be seen that the stress concentration remains at the crack tip while the interface crack propagates into the domain.

7. Conclusion

The dynamic interface crack propagation problem in a layered composite material has been studied. The orthotropic bi-material dynamic enrichment functions have been employed for reproducing the oscillatory stress and displacement fields near the interface crack tip. It has been observed that before crack growth, ignoring the oscillatory crack tip enrichments does not significantly affect the fracture mechanics parameters such as dynamic stress intensity factor and energy release rate; however, after crack growth, it results in spurious oscillations of the numerical response and inaccurate results. Also, it has been shown that neglecting the oscillatory crack tip enrichments decreases the accuracy of the solution in determining the crack tip velocity. Therefore, considering the oscillatory crack tip enrichment functions is very important in the dynamic crack propagation analysis. Moreover, it has been illustrated that using the time discontinuous finite element method for time integration of problems that include dynamic crack propagation is necessary for stabilizing the results. In addition, the balance of recovery algorithm has a remarkable effect in improving the results in these set

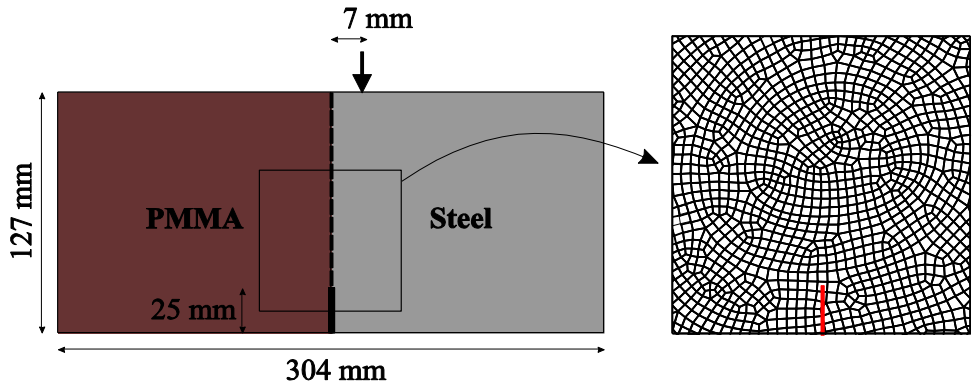

Fig. 19. Typical unstructured mesh around the crack tip.

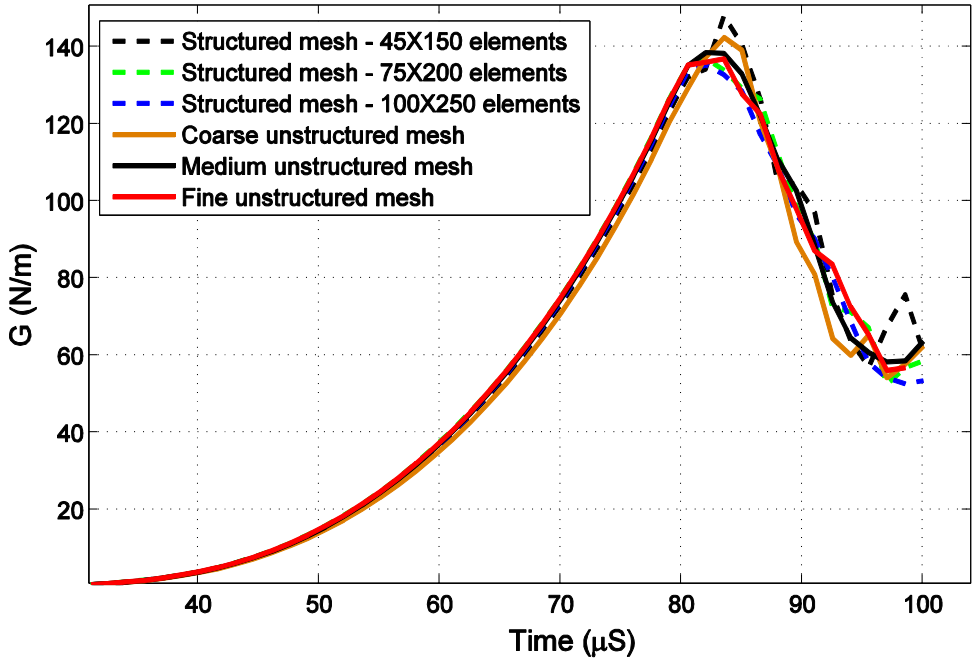

Fig. 20. Time history of energy release rate for structured and unstructured meshes.

Table 4
Material properties of the problem [61].

Parameter	Value	
	Homalite	Composite
E(GPa)	5.2	–
υ	0.34	–
ρ(kg/m^3)	7830	1478
$E_{\parallel}$(GPa)	–	80
$E_{\perp}$(GPa)	–	8.9
υ_{12}	–	0.25
G_{12}(GPa)	–	3.6

of problems. Finally, numerical simulations have proved that, among all the criteria proposed for dynamic interface crack growth, the criterion provided by Kavaturu and Shukla [52] is the only one that considers both the stable and the unstable crack growth processes and can completely predict the crack velocity through the solution.

The present mythology has so far been utilized only for mechanical loading conditions. Since the thermal shock dynamic analysis of cracked functionally graded piezoelectric solids was investigated using the extended finite element method [62], therefore, as an extension of the present work, the dynamic interface crack propagation problem under thermal shock loading conditions can also be studied."

Acknowledgments

The authors wish to gratefully acknowledge the technical support of the High Performance Computing Lab, School of Civil Engineering, University of Tehran. The financial support of Iran National Science Foundation (INSF) is gratefully acknowledged.

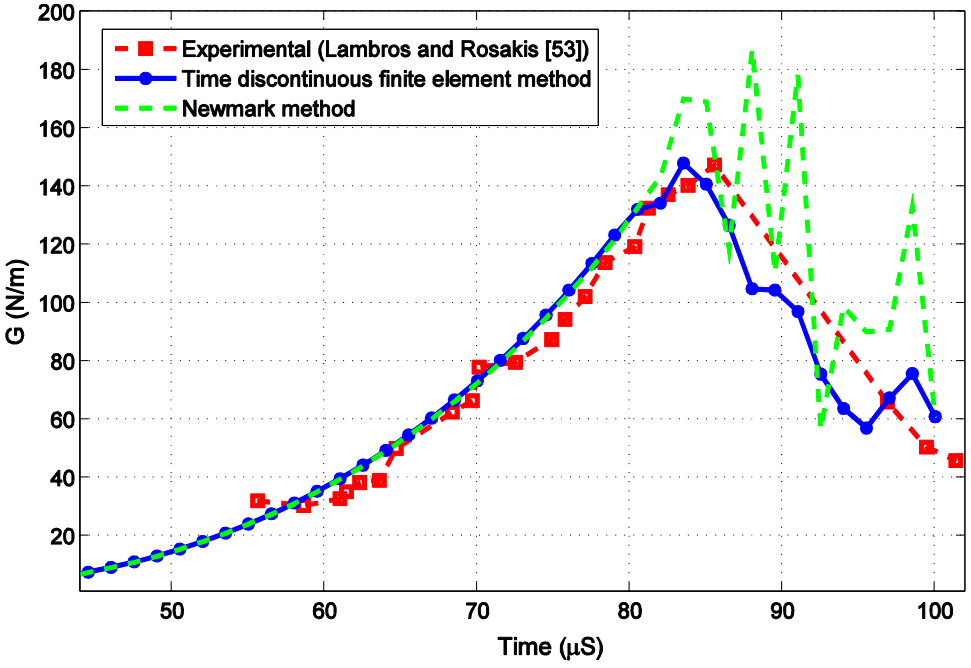

Fig. 21. Effect of the time integration method on the stability of the results.

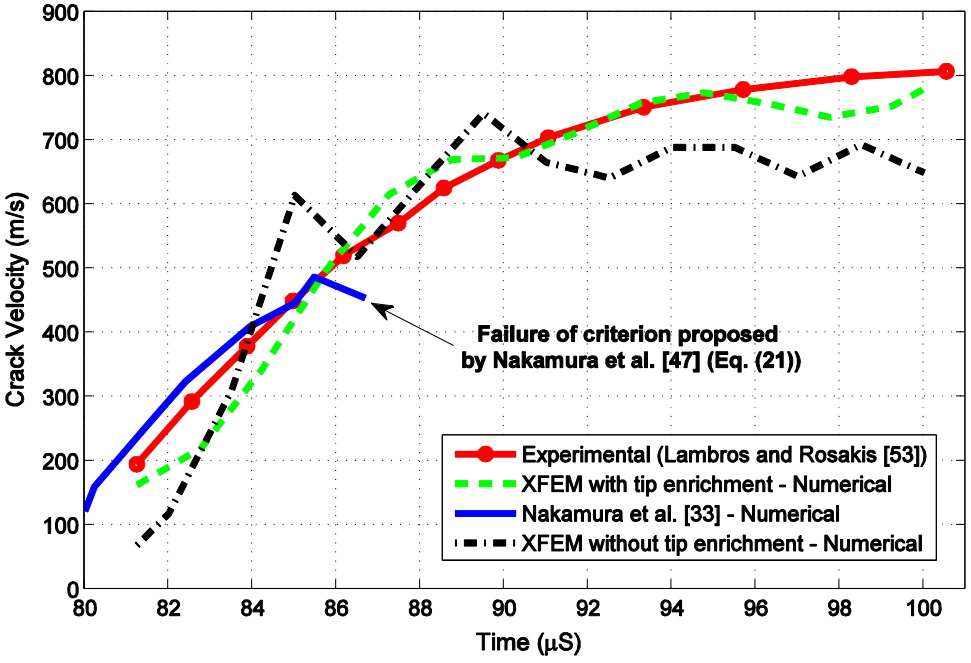

Fig. 22. The calculated crack tip velocity.

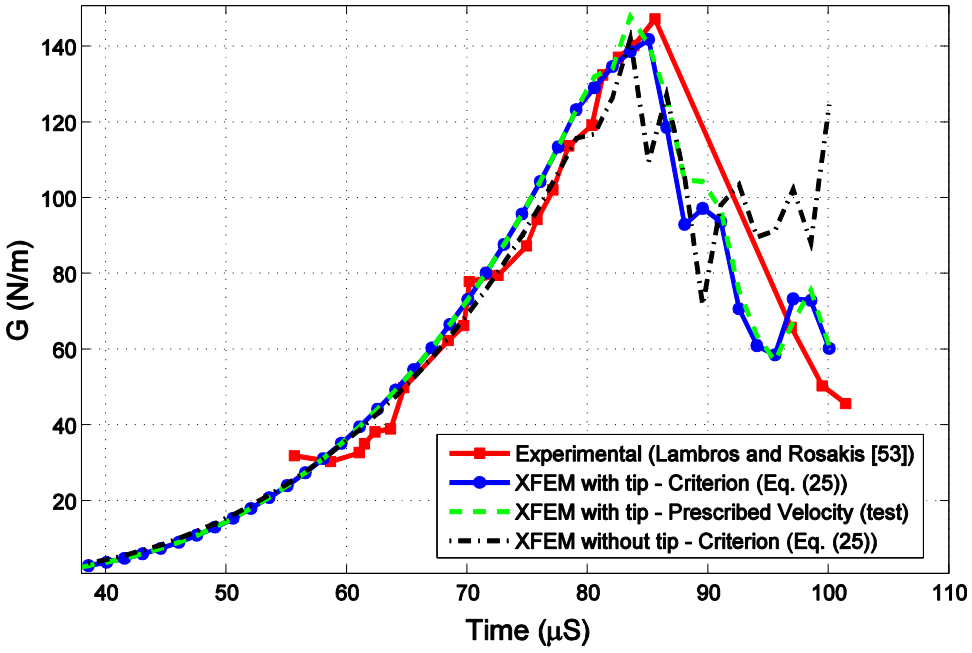

Fig. 23. Time variations of the energy release rate. (For interpretation of the references to color in this figure, the reader is referred to the web version of this article.)

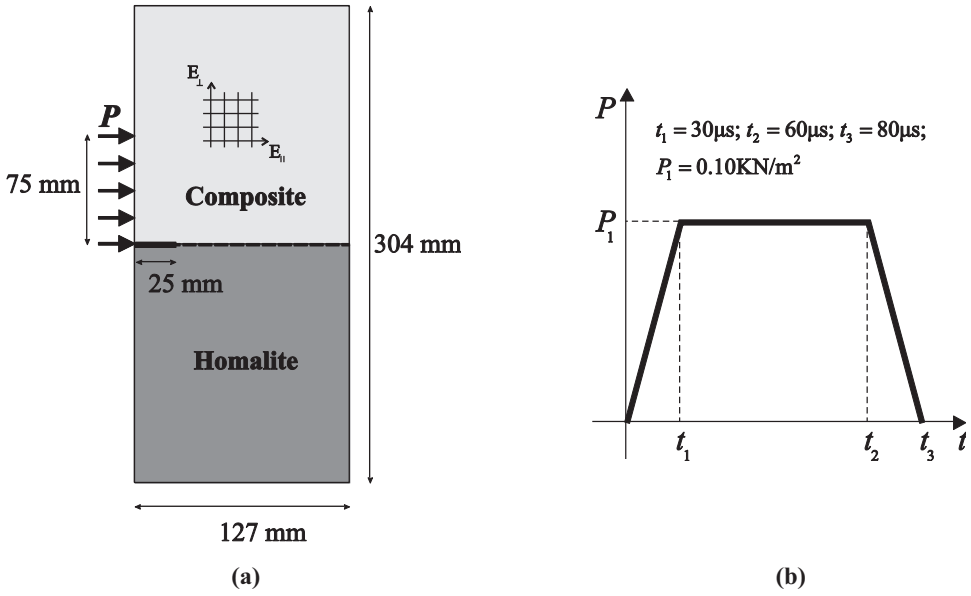

Fig. 24. (a) Geometry and dimensions of the model, (b) applied loading.

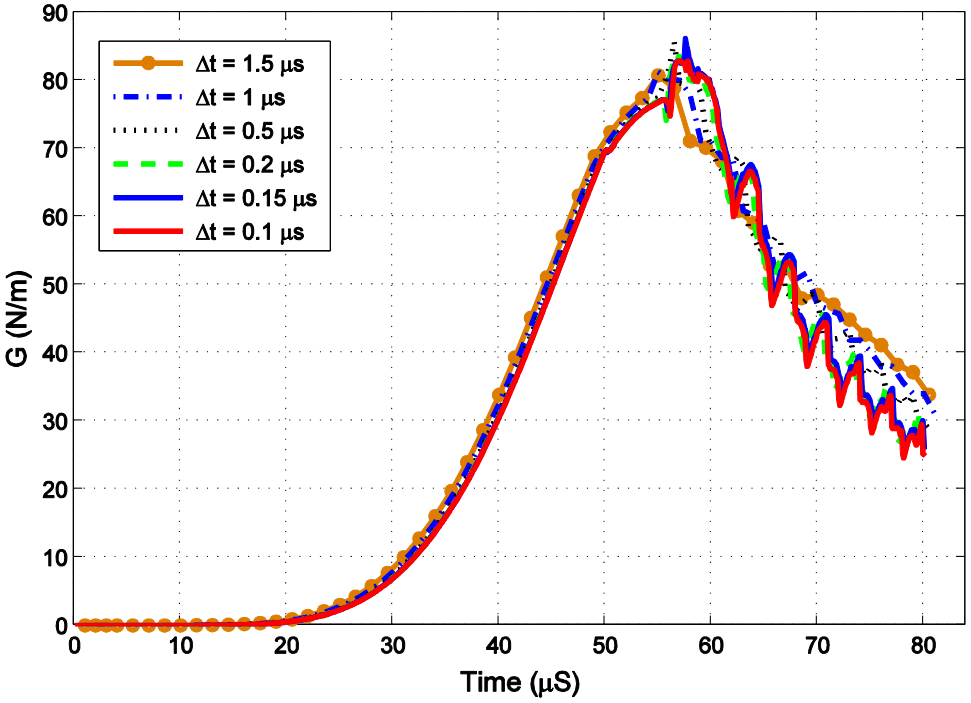

Fig. 25. Sensitivity of the energy release rate to the time step.

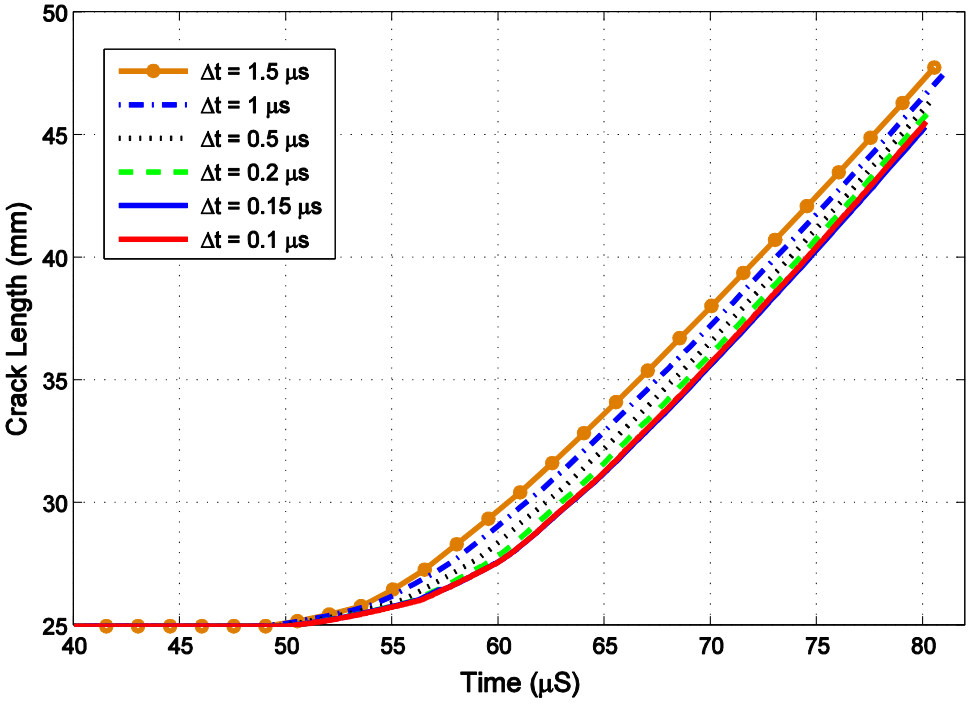

Fig. 26. Sensitivity of the crack length to the time step.

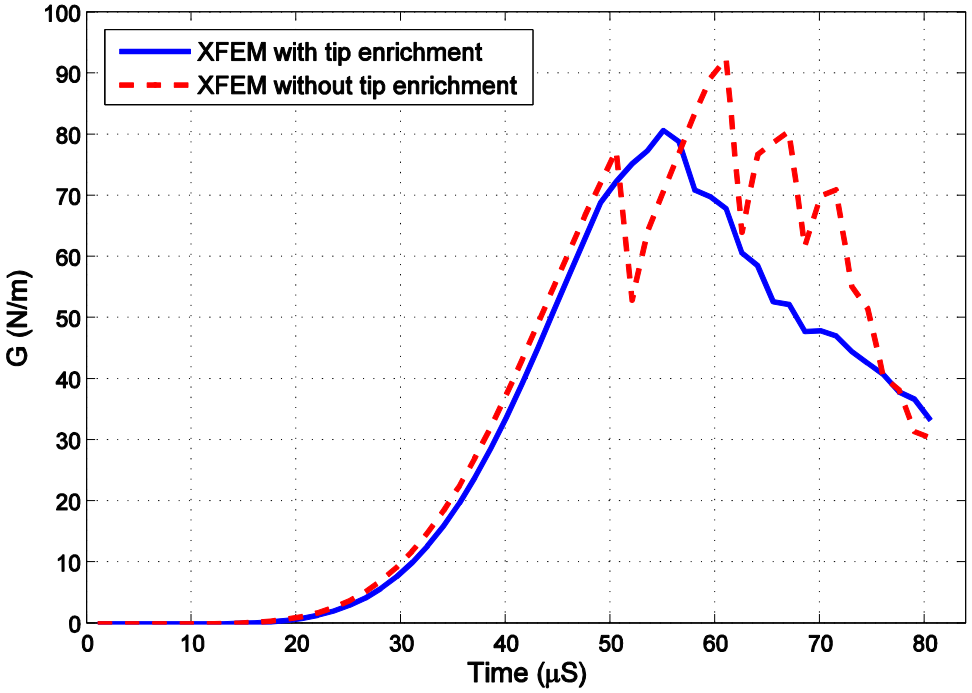

Fig. 27. Effect of oscillatory crack tip enrichments on the energy release rate.

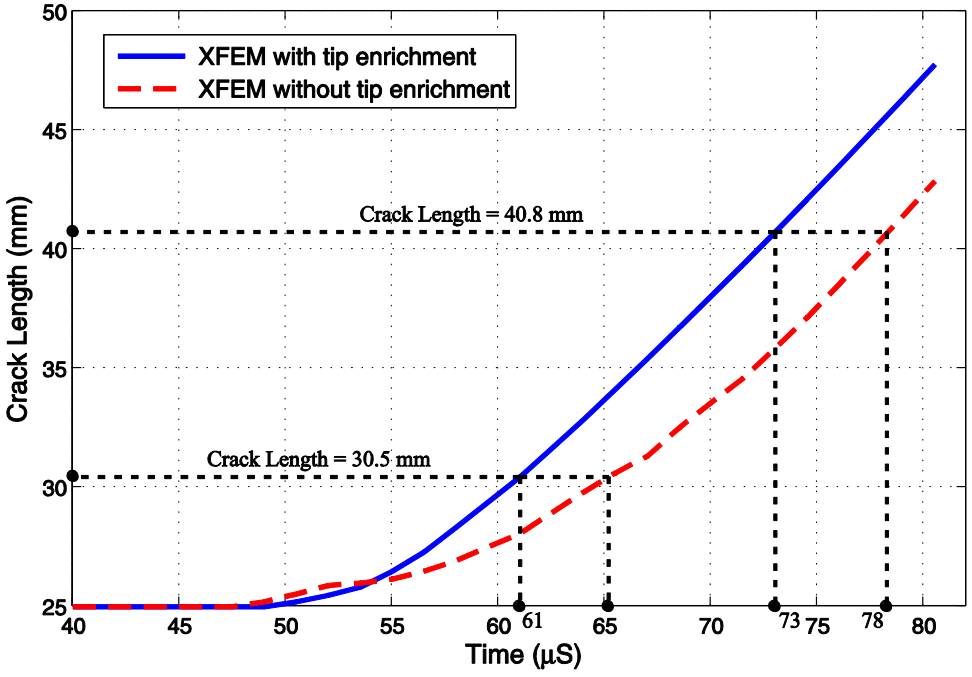

Fig. 28. Effect of oscillatory crack tip enrichments on the crack length.

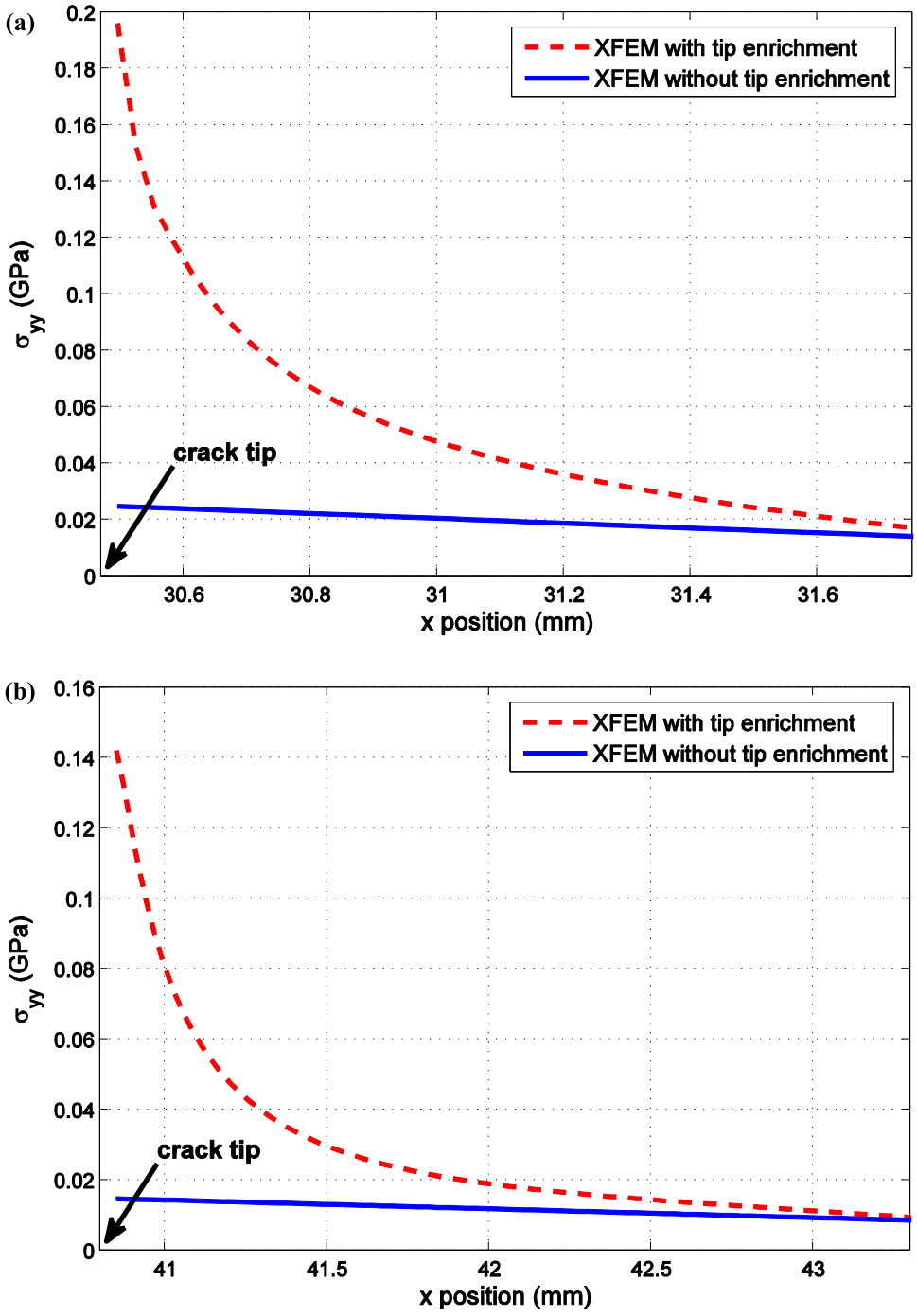

Fig. 29. Effect of oscillatory crack tip enrichments on the stress distribution near the crack tip, (a) crack length = 30.5 mm, (b) crack length = 40.8 mm.

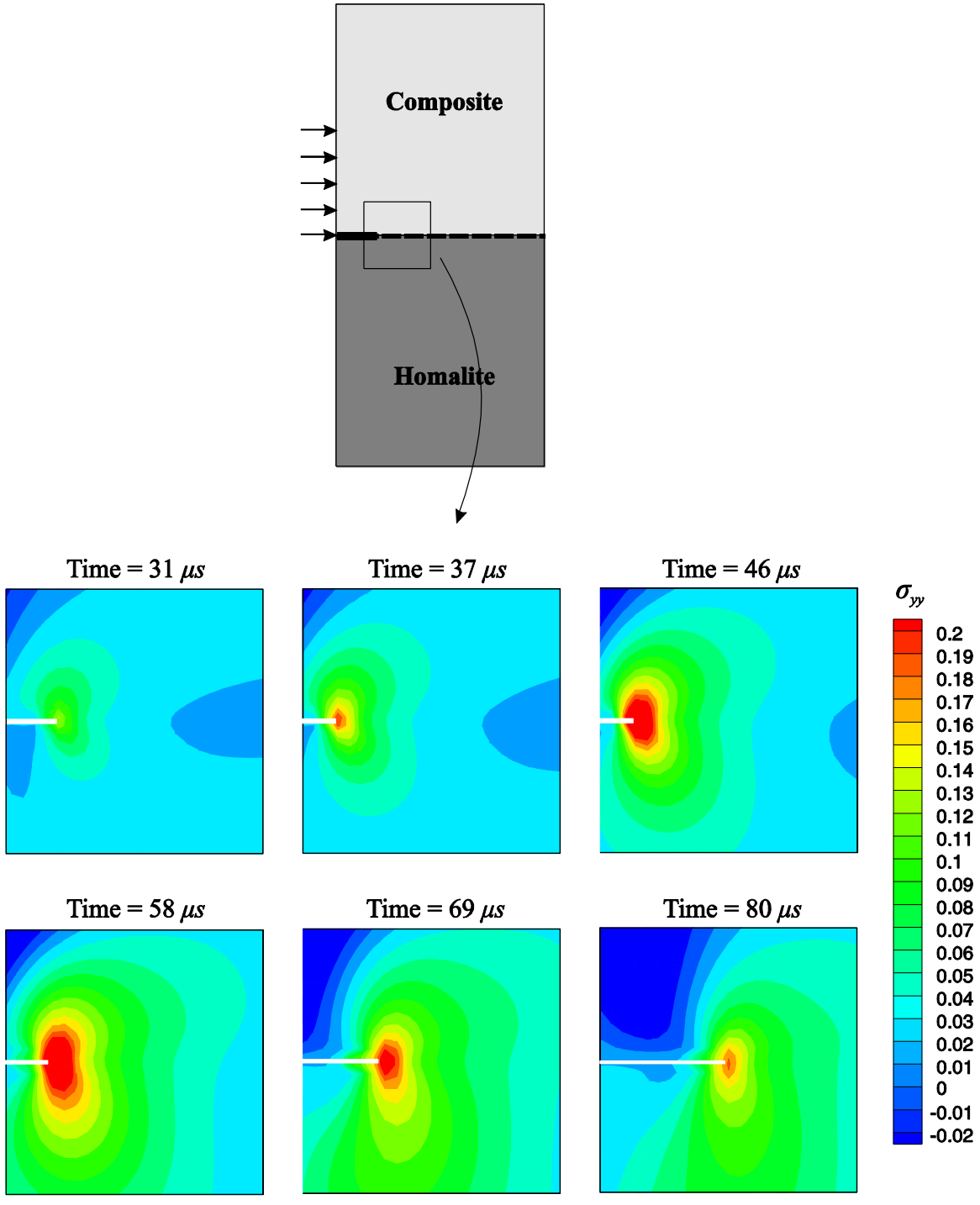

Fig. 30. Stress contours (σ_{yy}) at different times (stress in GPa).

Appendix A

The auxiliary stress and displacement fields around an interface crack tip in the upper material are presented in Eqs. (A.1)–(A.5) [63]. It should be noted that for the layer below the interface, $\varepsilon\pi$ and $-\varepsilon\pi$ are replaced with $-\varepsilon\pi$ and $\varepsilon\pi$, respectively.

$$\sigma_x = \frac{K_I}{2\sqrt{2\pi}D\cosh(\varepsilon\pi)} \times\Bigg[-p^2\Bigg\{e^{\varepsilon(\pi-\theta_l)}\bar{A}\cos\left(\varepsilon\ln(r_l)-\frac{\theta_l}{2}\right) +e^{-\varepsilon(\pi-\theta_l)}A\cos\left(\varepsilon\ln(r_l)+\frac{\theta_l}{2}\right)\Bigg\}(r_l)^{\frac{-1}{2}} +q^2\Bigg\{e^{\varepsilon(\pi-\theta_s)}\bar{B}\cos\left(\varepsilon\ln(r_s)-\frac{\theta_s}{2}\right) +e^{-\varepsilon(\pi-\theta_s)}B\cos\left(\varepsilon\ln(r_s)+\frac{\theta_s}{2}\right)\Bigg\}(r_s)^{\frac{-1}{2}}\Bigg] +\frac{K_{II}}{2\sqrt{2\pi}D\cosh(\varepsilon\pi)} \times\Bigg[p^2\Bigg\{e^{\varepsilon(\pi-\theta_l)}\bar{A}\sin\left(\varepsilon\ln(r_l)-\frac{\theta_l}{2}\right)$$

$$+e^{-\varepsilon(\pi-\theta_l)}A\sin\left(\varepsilon\ln(r_l)+\frac{\theta_l}{2}\right)\Big\}(r_l)^{\frac{-1}{2}}$$
$$-q^2\Big\{e^{\varepsilon(\pi-\theta_s)}\bar{B}\sin\left(\varepsilon\ln(r_s)-\frac{\theta_s}{2}\right)$$
$$+e^{-\varepsilon(\pi-\theta_s)}B\sin\left(\varepsilon\ln(r_s)+\frac{\theta_s}{2}\right)\Big\}(r_s)^{\frac{-1}{2}}\Big] \quad (A.1)$$

$$\sigma_y=\frac{K_I}{2\sqrt{2\pi}D\cosh(\varepsilon\pi)}$$
$$\times\Big[\Big\{e^{\varepsilon(\pi-\theta_l)}\bar{A}\cos\left(\varepsilon\ln(r_l)-\frac{\theta_l}{2}\right)$$
$$+e^{-\varepsilon(\pi-\theta_l)}A\cos\left(\varepsilon\ln(r_l)+\frac{\theta_l}{2}\right)\Big\}(r_l)^{\frac{-1}{2}}$$
$$-\Big\{e^{\varepsilon(\pi-\theta_s)}\bar{B}\cos\left(\varepsilon\ln(r_s)-\frac{\theta_s}{2}\right)$$
$$+e^{-\varepsilon(\pi-\theta_s)}B\cos\left(\varepsilon\ln(r_s)+\frac{\theta_s}{2}\right)\Big\}(r_s)^{\frac{-1}{2}}\Big]$$
$$+\frac{K_{II}}{2\sqrt{2\pi}D\cosh(\varepsilon\pi)}$$
$$\times\Big[\Big\{-e^{\varepsilon(\pi-\theta_l)}\bar{A}\sin\left(\varepsilon\ln(r_l)-\frac{\theta_l}{2}\right)$$
$$-e^{-\varepsilon(\pi-\theta_l)}A\sin\left(\varepsilon\ln(r_l)+\frac{\theta_l}{2}\right)\Big\}(r_l)^{\frac{-1}{2}}$$
$$+\Big\{e^{\varepsilon(\pi-\theta_s)}\bar{B}\sin\left(\varepsilon\ln(r_s)-\frac{\theta_s}{2}\right)$$
$$+e^{-\varepsilon(\pi-\theta_s)}B\sin\left(\varepsilon\ln(r_s)+\frac{\theta_s}{2}\right)\Big\}(r_s)^{\frac{-1}{2}}\Big] \quad (A.2)$$

$$\tau_{xy}=\frac{K_I}{2\sqrt{2\pi}D\cosh(\varepsilon\pi)}$$
$$\times\Big[\alpha_l\Big\{e^{\varepsilon(\pi-\theta_l)}\bar{A}\sin\left(\varepsilon\ln(r_l)-\frac{\theta_l}{2}\right)$$
$$-e^{-\varepsilon(\pi-\theta_l)}A\sin\left(\varepsilon\ln(r_l)+\frac{\theta_l}{2}\right)\Big\}(r_l)^{\frac{-1}{2}}$$
$$+\alpha_s\Big\{-e^{\varepsilon(\pi-\theta_s)}\bar{B}\sin\left(\varepsilon\ln(r_s)-\frac{\theta_s}{2}\right)$$
$$+e^{-\varepsilon(\pi-\theta_s)}B\sin\left(\varepsilon\ln(r_s)+\frac{\theta_s}{2}\right)\Big\}(r_s)^{\frac{-1}{2}}\Big]$$
$$+\frac{K_{II}}{2\sqrt{2\pi}D\cosh(\varepsilon\pi)}$$
$$\times\Big[\alpha_l\Big\{e^{\varepsilon(\pi-\theta_l)}\bar{A}\cos\left(\varepsilon\ln(r_l)-\frac{\theta_l}{2}\right)$$
$$-e^{-\varepsilon(\pi-\theta_l)}A\cos\left(\varepsilon\ln(r_l)+\frac{\theta_l}{2}\right)\Big\}(r_l)^{\frac{-1}{2}}$$
$$+\alpha_s\Big\{-e^{\varepsilon(\pi-\theta_s)}\bar{B}\cos\left(\varepsilon\ln(r_s)-\frac{\theta_s}{2}\right)$$
$$+e^{-\varepsilon(\pi-\theta_s)}B\cos\left(\varepsilon\ln(r_s)+\frac{\theta_s}{2}\right)\Big\}(r_s)^{\frac{-1}{2}}\Big] \quad (A.3)$$

$$u_x=\frac{K_I}{\sqrt{2\pi}(1+4\varepsilon^2)D\cosh(\varepsilon\pi)}$$
$$\times\Big\{e^{\varepsilon(\pi-\theta_l)}p_l\bar{A}\Big[\cos\left(\varepsilon\ln(r_l)-\frac{\theta_l}{2}\right)+2\varepsilon\sin\left(\varepsilon\ln(r_l)+\frac{\theta_l}{2}\right)\Big](r_l)^{\frac{1}{2}}$$
$$+e^{-\varepsilon(\pi-\theta_l)}p_lA\Big[\cos\left(\varepsilon\ln(r_l)-\frac{\theta_l}{2}\right)+2\varepsilon\sin\left(\varepsilon\ln(r_l)-\frac{\theta_l}{2}\right)\Big](r_l)^{\frac{1}{2}}\Big]$$
$$-e^{\varepsilon(\pi-\theta_s)}p_s\bar{B}\Big[\cos\left(\varepsilon\ln(r_s)+\frac{\theta_s}{2}\right)+2\varepsilon\sin\left(\varepsilon\ln(r_s)+\frac{\theta_s}{2}\right)\Big](r_s)^{\frac{1}{2}}$$
$$-e^{-\varepsilon(\pi-\theta_s)}p_sB\Big[\cos\left(\varepsilon\ln(r_s)-\frac{\theta_s}{2}\right)+2\varepsilon\sin\left(\varepsilon\ln(r_s)-\frac{\theta_s}{2}\right)\Big](r_s)^{\frac{1}{2}}\Big\}$$
$$+\frac{K_{II}}{\sqrt{2\pi}(1+4\varepsilon^2)D\cosh(\varepsilon\pi)}$$
$$\times\Big\{-e^{\varepsilon(\pi-\theta_l)}p_l\bar{A}\Big[\sin\left(\varepsilon\ln(r_l)+\frac{\theta_l}{2}\right)-2\varepsilon\cos\left(\varepsilon\ln(r_l)+\frac{\theta_l}{2}\right)\Big](r_l)^{\frac{1}{2}}$$
$$-e^{-\varepsilon(\pi-\theta_l)}p_lA\Big[\sin\left(\varepsilon\ln(r_l)-\frac{\theta_l}{2}\right)-2\varepsilon\cos\left(\varepsilon\ln(r_l)-\frac{\theta_l}{2}\right)\Big](r_l)^{\frac{1}{2}}\Big]$$
$$+e^{\varepsilon(\pi-\theta_s)}p_s\bar{B}\Big[\sin\left(\varepsilon\ln(r_s)+\frac{\theta_s}{2}\right)-2\varepsilon\cos\left(\varepsilon\ln(r_s)+\frac{\theta_s}{2}\right)\Big](r_s)^{\frac{1}{2}}$$
$$+e^{-\varepsilon(\pi-\theta_s)}p_sB\Big[\sin\left(\varepsilon\ln(r_s)-\frac{\theta_s}{2}\right)-2\varepsilon\cos\left(\varepsilon\ln(r_s)-\frac{\theta_s}{2}\right)\Big](r_s)^{\frac{1}{2}}\Big\} \quad (A.4)$$

$$u_y=\frac{K_I}{\sqrt{2\pi}(1+4\varepsilon^2)D\cosh(\varepsilon\pi)}$$
$$\times\Big\{e^{\varepsilon(\pi-\theta_l)}q_l\bar{A}\Big[\sin\left(\varepsilon\ln(r_l)+\frac{\theta_l}{2}\right)-2\varepsilon\cos\left(\varepsilon\ln(r_l)+\frac{\theta_l}{2}\right)\Big](r_l)^{\frac{1}{2}}$$
$$-e^{-\varepsilon(\pi-\theta_l)}q_lA\Big[\sin\left(\varepsilon\ln(r_l)-\frac{\theta_l}{2}\right)-2\varepsilon\cos\left(\varepsilon\ln(r_l)-\frac{\theta_l}{2}\right)\Big](r_l)^{\frac{1}{2}}\Big]$$
$$-e^{\varepsilon(\pi-\theta_s)}q_s\bar{B}\Big[\sin\left(\varepsilon\ln(r_s)+\frac{\theta_s}{2}\right)-2\varepsilon\cos\left(\varepsilon\ln(r_s)+\frac{\theta_s}{2}\right)\Big](r_s)^{\frac{1}{2}}$$
$$+e^{-\varepsilon(\pi-\theta_s)}q_sB\Big[\sin\left(\varepsilon\ln(r_s)-\frac{\theta_s}{2}\right)-2\varepsilon\cos\left(\varepsilon\ln(r_s)-\frac{\theta_s}{2}\right)\Big](r_s)^{\frac{1}{2}}\Big\}$$
$$+\frac{K_{II}}{\sqrt{2\pi}(1+4\varepsilon^2)D\cosh(\varepsilon\pi)}$$
$$\times\Big\{e^{\varepsilon(\pi-\theta_l)}q_l\bar{A}\Big[\cos\left(\varepsilon\ln(r_l)+\frac{\theta_l}{2}\right)+2\varepsilon\sin\left(\varepsilon\ln(r_l)+\frac{\theta_l}{2}\right)\Big](r_l)^{\frac{1}{2}}$$
$$-e^{-\varepsilon(\pi-\theta_l)}q_lA\Big[\cos\left(\varepsilon\ln(r_l)-\frac{\theta_l}{2}\right)+2\varepsilon\sin\left(\varepsilon\ln(r_l)-\frac{\theta_l}{2}\right)\Big](r_l)^{\frac{1}{2}}\Big]$$
$$-e^{\varepsilon(\pi-\theta_s)}q_s\bar{B}\Big[\cos\left(\varepsilon\ln(r_s)+\frac{\theta_s}{2}\right)+2\varepsilon\sin\left(\varepsilon\ln(r_s)+\frac{\theta_s}{2}\right)\Big](r_s)^{\frac{1}{2}}$$
$$+e^{-\varepsilon(\pi-\theta_s)}q_sB\Big[\cos\left(\varepsilon\ln(r_s)-\frac{\theta_s}{2}\right)+2\varepsilon\sin\left(\varepsilon\ln(r_s)-\frac{\theta_s}{2}\right)\Big](r_s)^{\frac{1}{2}}\Big\} \quad (A.5)$$

where

$$A=\alpha_s+\eta \quad (A.6)$$

$$\bar{A}=\alpha_s-\eta \quad (A.7)$$

$$B=\alpha_l+\eta \quad (A.8)$$

$$\bar{B}=\alpha_l-\eta \quad (A.9)$$

$$r_l=r\sqrt{\cos^2\theta+p^2\sin^2\theta} \quad (A.10)$$

$$r_s=r\sqrt{\cos^2\theta+q^2\sin^2\theta} \quad (A.11)$$

$$\theta_j=\tan^{-1}(Z_j\tan\theta),\ j=l,s,\ Z_l=p,\ Z_s=q \quad (A.12)$$

In order to calculate Eqs. (A.6)–(A.12), polar coordinates $(r,\ \theta)$ in front of the crack tip is used (see Fig. 1). In Eqs. (A.6)–(A.12), parameters α_s, α_l, p, q, η are defined as follow:

$$p=\sqrt{B_{12}-\sqrt{B_{12}^2-K_{66}}} \quad (A.13)$$

$$q = \sqrt{B_{12} + \sqrt{B_{12}^2 - K_{66}}} \tag{A.14}$$

$$B_{12} = \frac{1}{2a_{11}}\left\{2a_{12} + a_{66} + \rho V^2\left(a_{12}^2 - a_{11}a_{66} - a_{11}a_{22}\right)\right\} \tag{A.15}$$

$$K_{66} = \frac{1}{a_{11}}\left\{a_{22} + \rho V^2\left(a_{12}^2 - a_{22}a_{66} - a_{11}a_{22} + \rho V^2 a_{66}\left(a_{11}a_{22} - a_{12}^2\right)\right)\right\} \tag{A.16}$$

$$\alpha_s = q + a_{22}\frac{\rho V^2}{q} - q\rho V^2 a_{11} - \frac{\left(\rho V^2\right)^2}{q}\left(a_{11}a_{22} - a_{12}^2\right) \tag{A.17}$$

$$\alpha_l = p + a_{22}\frac{\rho V^2}{p} - p\rho V^2 a_{11} - \frac{\left(\rho V^2\right)^2}{p}\left(a_{11}a_{22} - a_{12}^2\right) \tag{A.18}$$

where a_{ij} are the components of the compliance tensor, V is the crack velocity, and ρ is the density.

References

[1] Doan DH, Bui TQ, Duc ND, Fushinobu K. Hybrid phase field simulation of dynamic crack propagation in functionally graded glass-filled epoxy. Compos Part B Eng 2016;99:266–76.
[2] Hao W, Tang C, Yuan Y, Ma Y. Investigation of dynamic mode I matrix crack-fiber bundle interaction in composites using caustics. Compos Part B Eng 2016;92:395–404.
[3] Hutchinson JW, Mear M, Rice JR. Crack paralleling an interface between dissimilar materials. J Appl Mech 1987;54:828–32.
[4] Kang Z, Bui TQ, Hirose S. Dynamic stationary crack analysis of isotropic solids and anisotropic composites by enhanced local enriched consecutive-interpolation elements. Compos Struct 2017;180:221–33.
[5] Lee D, Tippur H, Bogert P. Quasi-static and dynamic fracture of graphite/epoxy composites: An optical study of loading-rate effects. Compos Part B Eng 2010;41:462–74.
[6] Nguyen MN, Bui TQ, Nguyen NT, Truong TT, Van Lich L. Simulation of dynamic and static thermoelastic fracture problems by extended nodal gradient finite elements. Int J Mech Sci 2017;134:370–86.
[7] Rice J. Elastic fracture mechanics concepts for interfacial cracks. J Appl Mech 1988;55:98–103.
[8] Belytschko T, Black T. Elastic crack growth in finite elements with minimal remeshing. Int J Numer Methods Eng 1999;45:601–20.
[9] Bui TQ. Extended isogeometric dynamic and static fracture analysis for cracks in piezoelectric materials using NURBS. Comput Methods Appl Mech Eng 2015;295:470–509.
[10] Bui TQ, Hirose S, Zhang C, Rabczuk T, Wu C-T, Saitoh T, Lei J. Extended isogeometric analysis for dynamic fracture in multiphase piezoelectric/piezomagnetic composites. Mech Mater 2016;97:135–63.
[11] Ghorashi SS, Valizadeh N, Mohammadi S. Extended isogeometric analysis for simulation of stationary and propagating cracks. Int J Numer Methods Eng 2012;89:1069–101.
[12] Singh S, Singh I, Mishra B, Bhardwaj G, Bui T. A simple, efficient and accurate Bézier extraction based T-spline XIGA for crack simulations. Theor Appl Fract Mech 2017;88:74–96.
[13] Ambati M, Kruse R, De Lorenzis L. A phase-field model for ductile fracture at finite strains and its experimental verification. Comput Mech 2016;57:149–67.
[14] Doan DH, Bui TQ, Van Do T, Duc ND. A rate-dependent hybrid phase field model for dynamic crack propagation. J Appl Phys 2017;122:115102.
[15] Asadpoure A, Mohammadi S. Developing new enrichment functions for crack simulation in orthotropic media by the extended finite element method. Int J Numer Methods Eng 2007;69:2150–72.
[16] Esna Ashari S, Mohammadi S. Delamination analysis of composites by new orthotropic bimaterial extended finite element method. Int J Numer Methods Eng 2011;86:1507–43.
[17] Liu X, Xiao Q, Karihaloo BL. XFEM for direct evaluation of mixed mode SIFs in homogeneous and bi-materials. Int J Numer Methods Eng 2004;59:1103–18.
[18] Nagashima T, Omoto Y, Tani S. Stress intensity factor analysis of interface cracks using X-FEM. Int J Numer Methods Eng 2003;56:1151–73.
[19] Nasirmanesh A, Mohammadi S. XFEM buckling analysis of cracked composite plates. Compos Struct 2015;131:333–43.
[20] Nasirmanesh A, Mohammadi S. Eigenvalue buckling analysis of cracked functionally graded cylindrical shells in the framework of the extended finite element method. Compos Struct 2017;159:548–66.
[21] Natarajan S, Baiz PM, Bordas S, Rabczuk T, Kerfriden P. Natural frequencies of cracked functionally graded material plates by the extended finite element method. Compos Struct 2011;93:3082–92.
[22] I. Singh, B. Mishra, S. Bhattacharya, XFEM simulation of cracks, holes and inclusions in functionally graded materials, Int J Mech Mater Des, 7 (2011) 199.
[23] Yu T, Bui TQ, Liu P, Zhang C, Hirose S. Interfacial dynamic impermeable cracks analysis in dissimilar piezoelectric materials under coupled electromechanical loading with the extended finite element method. Int J Solids Struct 2015;67:205–18.
[24] Afshar A, Ardakani SH, Mohammadi S. Transient analysis of stationary interface cracks in orthotropic bi-materials using oscillatory crack tip enrichments. Compos Struct 2016.
[25] Afshar A, Ardakani SH, Hashemi S, Mohammadi S. Numerical analysis of crack tip fields in interface fracture of SMA/elastic bi-materials. Int J Fract 2015;195:39–52.
[26] Bui TQ, Zhang C. Extended finite element simulation of stationary dynamic cracks in piezoelectric solids under impact loading. Comput Mater Sci 2012;62:243–57.
[27] Bui TQ, Zhang C. Analysis of generalized dynamic intensity factors of cracked magnetoelectroelastic solids by X-FEM. Finite Elem Anal Des 2013;69:19–36.
[28] Liu P, Yu T, Bui TQ, Zhang C. Transient dynamic crack analysis in non-homogeneous functionally graded piezoelectric materials by the X-FEM. Comput Mater Sci 2013;69:542–58.
[29] Ardakani SH, Ahmadian H, Mohammadi S. Thermo-mechanically coupled fracture analysis of shape memory alloys using the extended finite element method. Smart Mater Struct 2015;24:045031.
[30] Kumar S, Singh I, Mishra B. A homogenized XFEM approach to simulate fatigue crack growth problems. Comput Struct 2015;150:1–22.
[31] Kumar S, Singh I, Mishra B, Sharma K, Khan I. A homogenized multigrid XFEM to predict the crack growth behavior of ductile material in the presence of microstructural defects. Eng Fract Mech 2016.
[32] Belytschko T, Chen H, Xu J, Zi G. Dynamic crack propagation based on loss of hyperbolicity and a new discontinuous enrichment. Int J Numer Methods Eng 2003;58:1873–905.
[33] Chessa J, Belytschko T. Arbitrary discontinuities in space–time finite elements by level sets and X-FEM. Int J Numer Methods Eng 2004;61:2595–614.
[34] Chessa J, Belytschko T. A local space–time discontinuous finite element method. Comput Methods Appl Mech Eng 2006;195:1325–43.
[35] Belytschko T, Chen H. Singular enrichment finite element method for elastodynamic crack propagation. Int J Comput Methods 2004;1:1–15.
[36] Grégoire D, Maigre H, Rethore J, Combescure A. Dynamic crack propagation under mixed-mode loading – comparison between experiments and X-FEM simulations. Int J Solids Struct 2007;44:6517–34.
[37] Haboussa D, Grégoire D, Elguedj T, Maigre H, Combescure A. X-FEM analysis of the effects of holes or other cracks on dynamic crack propagations. Int J Numer Methods Eng 2011;86:618–36.
[38] Combescure A, Gravouil A, Grégoire D, Rethore J. X-FEM a good candidate for energy conservation in simulation of brittle dynamic crack propagation. Comput Methods Appl Mech Eng 2008;197:309–18.
[39] Menouillard T, Rethore J, Moes N, Combescure A, Bung H. Mass lumping strategies for X-FEM explicit dynamics: application to crack propagation. Int J Numer Methods Eng 2008;74:447–74.
[40] Motamedi D, Mohammadi S. Fracture analysis of composites by time independent moving-crack orthotropic XFEM. Int J Mech Sci 2012;54:20–37.
[41] Motamedi D, Mohammadi S. Dynamic crack propagation analysis of orthotropic media by the extended finite element method. Int J Fract 2010;161:21–39.
[42] Kumar S, Singh I, Mishra B, Singh A. New enrichments in XFEM to model dynamic crack response of 2-D elastic solids. Int J Impact Eng 2016;87:198–211.
[43] Li X, Yao D, Lewis R. A discontinuous Galerkin finite element method for dynamic and wave propagation problems in non-linear solids and saturated porous media. Int J Numer Methods Eng 2003;57:1775–800.
[44] Rethore J, Gravouil A, Combescure A. A combined space–time extended finite element method. Int J Numer Methods Eng 2005;64:260–84.
[45] Lekhnitskii S. Theory of elasticity of an anisotropic elastic body. San Francisco: Holden-Day; 1963.
[46] Cho SB, Lee KR, Choy YS, Ryoji Y. Determination of stress intensity factors and boundary element analysis for interface cracks in dissimilar anisotropic materials. Eng Fract Mech 1992;43:603–14.
[47] Nakamura T, Kushner A, Lo C. Interlaminar dynamic crack propagation. Int J Solids Struct 1995;32:2657–75.
[48] Kim J-H, Paulino GH. The interaction integral for fracture of orthotropic functionally graded materials: evaluation of stress intensity factors. Int J Solids Struct 2003;40:3967–4001.
[49] Song SH, Paulino GH. Dynamic stress intensity factors for homogeneous and smoothly heterogeneous materials using the interaction integral method. Int J Solids Struct 2006;43:4830–66.
[50] Li FZ, Shih CF, Needleman A. A comparison of methods for calculating energy release rates. Eng Fract Mech 1985;21:405–21.
[51] Singh RP, Kavaturu M, Shukla A. Initiation, propagation and arrest of an interface crack subjected to controlled stress wave loading. Int J Fract 1997;83:291–304.
[52] Kavaturu M, Shukla A. Dynamic fracture criteria for crack growth along bimaterial interfaces. J Appl Mech 1998;65:293–9.
[53] Lambros J, Rosakis AJ. Dynamic decohesion of bimaterials: experimental observations and failure criteria. Int J Solids Struct 1995;32:2677–702.
[54] Mohammadi S. Extended finite element method: For fracture analysis of structures. UK: Blackwell Publishing; 2008.
[55] Nguyen-Vinh H, Bakar I, Msekh M, Song J-H, Muthu J, Zi G, Le P, Bordas SPA, Simpson R, Natarajan S. Extended finite element method for dynamic fracture of piezo-electric materials. Eng Fract Mech 2012;92:19–31.
[56] Zienkiewicz OC. A new look at the Newmark, Houbolt and other time stepping formulas. A weighted residual approach. Earthq Eng Struct Dyn 1977;5:413–18.
[57] Afshar A, Daneshyar A, Mohammadi S. XFEM analysis of fiber bridging in mixed–mode crack propagation in composites. Compos Struct 2015;125:314–27.
[58] Rethore J, Gravouil A, Combescure A. A stable numerical scheme for the finite element simulation of dynamic crack propagation with remeshing. Comput Methods Appl Mech Eng 2004;193:4493–510.

[59] Liu Z, Menouillard T, Belytschko T. An XFEM/spectral element method for dynamic crack propagation. Int J Fract 2011;169:183–98.
[60] Freund LB. Dynamic fracture mechanics. New York: Cambridge University Press; 1998.
[61] Coker D, Rosakis A, Needleman A. Dynamic crack growth along a polymer composite–Homalite interface. J Mech Phys Solids 2003;51:425–60.
[62] Liu P, Yu T, Bui TQ, Zhang C, Xu Y, Lim CW. Transient thermal shock fracture analysis of functionally graded piezoelectric materials by the extended finite element method. Int J Solids Struct 2014;51:2167–82.
[63] Lee K. Stress and displacement fields for propagating the crack along the interface of dissimilar orthotropic materials under dynamic mode I and II load. J Appl Mech 2000;67:223–8.